Bioactive Materials 20 (2023) 221–242

Contents lists available at ScienceDirect

Bioactive Materials

journal homepage: www.keaipublishing.com/en/journals/bioactive-materials

Silk-based hydrogel incorporated with metal-organic framework nanozymes for enhanced osteochondral regeneration

Zhicheng Cao [a,b,1], Hongmei Wang [b,c,1], Jialin Chen [b,d,e,1], Yanan Zhang [b], Qingyun Mo [b], Po Zhang [a,b], Mingyue Wang [b], Haoyang Liu [b], Xueyang Bao [b], Yuzhi Sun [a,b], Wei Zhang [b,d,e,**], Qingqiang Yao [a,e,*]

[a] Department of Orthopaedic Surgery, Institute of Digital Medicine, Nanjing First Hospital, Nanjing Medical University, 210006, Nanjing, China
[b] School of Medicine, Southeast University, 210009, Nanjing, China
[c] Department of Pharmaceutical Sciences, Binzhou Medical University, 264003, Yantai, Shandong, China
[d] Jiangsu Key Laboratory for Biomaterials and Devices, Southeast University, 210096, Nanjing, China
[e] China Orthopedic Regenerative Medicine Group (CORMed), China

ARTICLE INFO

Keywords:
Osteochondral regeneration
Metal-organic framework
Nanozyme
Inflammation
ROS
Silk

ABSTRACT

Osteochondral defects (OCD) cannot be efficiently repaired due to the unique physical architecture and the pathological microenvironment including enhanced oxidative stress and inflammation. Conventional strategies, such as the control of implant microstructure or the introduction of growth factors, have limited functions failing to manage these complex environments. Here we developed a multifunctional silk-based hydrogel incorporated with metal-organic framework nanozymes (CuTA@SF) to provide a suitable microenvironment for enhanced OCD regeneration. The incorporation of CuTA nanozymes endowed the SF hydrogel with a uniform microstructure and elevated hydrophilicity. In vitro cultivation of mesenchymal stem cells (MSCs) and chondrocytes showed that CuTA@SF hydrogel accelerated cell proliferation and enhanced cell viability, as well as had antioxidant and antibacterial properties. Under the inflammatory environment with the stimulation of IL-1β, CuTA@SF hydrogel still possessed the potential to promote MSC osteogenesis and deposition of cartilage-specific extracellular matrix (ECM). The proteomics analysis further confirmed that CuTA@SF hydrogel promoted cell proliferation and ECM synthesis. In the full-thickness OCD model of rabbit, CuTA@SF hydrogel displayed successfully in situ OCD regeneration, as evidenced by micro-CT, histology (HE, S/O, and toluidine blue staining) and immunohistochemistry (Col I and aggrecan immunostaining). Therefore, CuTA@SF hydrogel is a promising biomaterial targeted at the regeneration of OCD.

1. Introduction

Cartilage plays an irreplaceable role in the musculoskeletal system for its lubricating and shock-absorbing properties. Attributed to the trauma, increasing fitness activity and age-related degeneration, cartilage injury is one of the most common types of musculoskeletal injuries. Clinically, it is of great challenge to repair injured cartilage due to its unique physical architecture and poor nutrition supplement [1]. Additionally, cartilage has a close link with the subchondral bone. Changes in local biomechanics and loss of protective ability after cartilage injury usually induce subchondral bone destruction, termed osteochondral defect (OCD), which is quite possible to develop into post-trauma osteoarthritis in the future. Whereas, the simultaneous regeneration of cartilage and subchondral bone is of great difficulty as an entirely different physiological nature of these two layers [2]. Subchondral drilling, microfracture and autologous chondrocyte implantation (ACI) are employed in the treatment of cartilage injury at present. Although these treatments can relieve the patient's pain and partially restore

Peer review under responsibility of KeAi Communications Co., Ltd.

* Corresponding author. Department of Orthopaedic Surgery, Institute of Digital Medicine, Nanjing First Hospital, Nanjing Medical University, 210006, Nanjing, China.
** Corresponding author. School of Medicine, Southeast University, 210009, Nanjing, China.
E-mail addresses: zhang.wei@seu.edu.cn (W. Zhang), yaoqingqiang@njmu.edu.cn (Q. Yao).
[1] These co-authors contributed equally to this work.

https://doi.org/10.1016/j.bioactmat.2022.05.025
Received 7 March 2022; Received in revised form 2 May 2022; Accepted 19 May 2022

cartilage defects, limited application, donor site morbidity, indistinct long-term effects and allogeneic rejection are the matters desired to be solved [3].

To date, it has been established that OCD is not just a disease confined to the injured site. The onset of defects affects the microenvironment of the whole joint [4,5]. After OCD, an acute inflammatory response occurs in the joint [6,7]. Previous studies have identified the overexpression of interleukin-1β (IL-1β) in the surrounding tissues of the defect [8,9]. The local inflammatory microenvironment has been proved to be a barrier to osteogenic and chondrogenic differentiation of mesenchymal stem cells (MSCs) [10–12]. At the same time, reactive oxygen species (ROS) are generated and tightly associated with the presence of the inflammatory microenvironment. Increased intracellular ROS levels would be detected after inflammatory factor stimulates, which subsequently contribute to the secretion of matrix-degrading enzymes, such as matrix metalloproteinases (MMPs) and ADAMTS (a disintegrin and metalloproteinase with thrombospondin motifs) [11,13,14]. ROS reduces the efficiency of osteogenic differentiation of MSCs [15,16] and induces the transition of chondrocytes to a hypertrophic phenotype [17]. Researchers have found that some antioxidants can regulate the expression of antioxidant enzymes like superoxide dismutase (SOD) and heme oxygenase-1 (HO-1) through NF-E2-related Factor 2 (Nrf2) pathway, thus the balance between oxidation and anti-oxidation in the microenvironment will be maintained [18,19]. Collectively, excessive inflammatory factors and ROS are tightly associated with the aggravated microenvironment after OCD, and this will lead to cartilage extracellular matrix (ECM) degeneration and impede OCD regeneration. The incidence of post-traumatic osteoarthritis will increase in this hostile environment [14], causing irreversible damage to the structure and function of the entire joint. Consequently, it is of great importance to alleviate ROS and inflammatory factors in the microenvironment of OCD for enhanced regeneration.

Recently, tissue engineering methods, by adopting suitable biomaterials and biomolecules, have shown promises for modifying the in situ microenvironment, including targeting at ROS and inflammatory reaction following OCD [20]. Tannic acid (TA), a natural polyphenolic compound derived from plants, is growingly applied to tissue engineering applications. TA not only can act as a surface modifier through various chemical bonds like hydrogen bonds, coordination bonds, ionic bonds and van der Waals forces, but also possess biological properties such as antioxidant, anti-inflammation and antibacterial effects [21,22]. As a surface modifier, the incorporation of TA could control the microstructure of the material. He X et al. reported that the addition of TA to the photo-crosslinked silk fibroin (SF) could reduce the pore size while improving the mechanical strength of the hydrogel [23]. Furthermore, we and other researchers have found that the surface modification with TA can enhance the stability of the base materials, realizing the controlled release of small molecules [24–26]. Plant-derived phenolic acids were also applied to the synthesis of nanoparticles as a reducing agent. Polyphenolic modified nanoparticles possess excellent antioxidant activities and have good dispersibility avoiding cytotoxicity caused by aggregation [27]. It has been reported that TA can decrease intracellular ROS levels upon hydrogen peroxide stimulation [28,29], indicating that TA has the potential to protect cells from oxidative stress-induced harmful effects. Additionally, due to the rich galloyl group, TA is also considered to be an effective spectral antibacterial molecule [30].

As a trace element, copper exerts an essential function in the structural composition and physiological activities of the human body. It has been reported that copper-containing biomaterials such as hydrogel and nanoparticles accelerate cell proliferation, thereby promoting tissue regeneration [31–33]. In addition, copper-containing ceramic contributed to the polarization of macrophages towards the M2 phenotype and exerted an anti-inflammatory effect in OCD regeneration [34]. Copper-dependent enzymes, like Cu-ZnSOD and Ceruloplasmin, are indispensable components of the organism to scavenge ROS under the oxidative stress environment [35–37]. Recently, copper-based nanomaterials with enzyme-like activities (nanozymes) have attracted much attention in the field of biomedicine. Lin et al. designed a metal-organic framework (MOF) nanozyme that combined copper ion and TA. The strong coordination interaction between copper ions and the TA organic ligands enables the formation of a unique crystalline structure with high stability, exhibiting excellent SOD-like activity for scavenging ROS in cigarette smoke and reducing oxidative stress-induced lung inflammation [38]. Hence, we infer that the MOF nanozyme comprising of copper nanoparticles and TA (CuTA nanozyme) may promote OCD regeneration through scavenging ROS and moderating inflammation.

In this present study, a silk-based hydrogel incorporated with CuTA nanozyme, i.e., CuTA@SF hydrogel, was developed to ameliorate oxidative stress and inflammation to provide a suitable microenvironment for OCD regeneration (Scheme 1). SF is one of the FDA and CFDA approved biomaterials and has been widely used in tissue engineering applications [39,40]. Our study tries to take advantage of CuTA nanozyme and SF to fabricate a novel multifunction CuTA@SF hydrogel to promote the in-situ regeneration of OCD. The combination of SF and TA through hydrogen bond forms a uniform network structure, in which TA-modified copper nanoparticles can disperse well. The morphological and physicochemical properties of CuTA@SF hydrogel were systematically characterized by a series of in vitro experiments. In addition, the biological properties of CuTA@SF hydrogel, including cytocompatibility, antioxidant activity, pro-differentiation capacity as well as the activity of modulating the local inflammatory environment, were evaluated by using bone marrow-derived mesenchymal stem cells (BMSCs) and chondrocytes. Proteomic analysis was further performed to detect the involved pathways and mechanisms of cell behavior affected by the CuTA@SF hydrogel. Finally, the CuTA@SF hydrogel was implanted into a rabbit femoral osteochondral defect model to evaluate its ability to promote OCD regeneration in vivo.

2. Materials and methods

2.1. Preparation of SF solution

First, raw silk fibers (Zhejiang Xingyue Biotechnology Co. Ltd, China) were boiled in 0.02 M of Na_2CO_3 (Sinopharm, China) solution for 0.5 h and rinsed in distilled water. The obtained fibroin was dried in an oven at 37 °C overnight and dissolved in a lithium bromide (Macklin, China) solution. Then the solution was transferred to a dialysis bag (Shanghai yuanye Bio-Technology Co., Ltd., China) and dialyzed against deionized water for two days. Centrifugation was performed twice at 9000 rpm at 4 °C for 20 min. The resulting supernatant was collected and stored at 4 °C.

2.2. The synthesis and characterization of CuTA nanozyme (Fourier transform infrared spectroscopy (FTIR), X-ray diffraction (XRD) and thermogravimetry (TG) analysis)

12.8 mg copper nanoparticles (Sigma-Aldrich) and 10 mg TA (Sigma-Aldrich) powder were added to 1 ml deionized water. After Shaking at 37 °C for 24 h, the obtained solution was centrifuged to collect the precipitate. The precipitate was washed thoroughly with deionized water three times and then dried at 37 °C to get the powder of CuTA.

Copper nanoparticles, TA and CuTA were used for FTIR (Nicolet iS50 FT-IR, Thermo Fisher, USA), XRD (Bruker D8-Advance, Germany) and TG (SDT-Q600, TA, USA) analysis.

2.3. The coating efficiency and durability of CuTA nanozyme

The coating efficiency and durability of TA were evaluated with the Enhanced BCA Protein Assay Kit (Beyotime, China) as previously reported [25]. Briefly, we collected the supernatant during the process of CuTA synthesis and the solution was subsequently detected with a

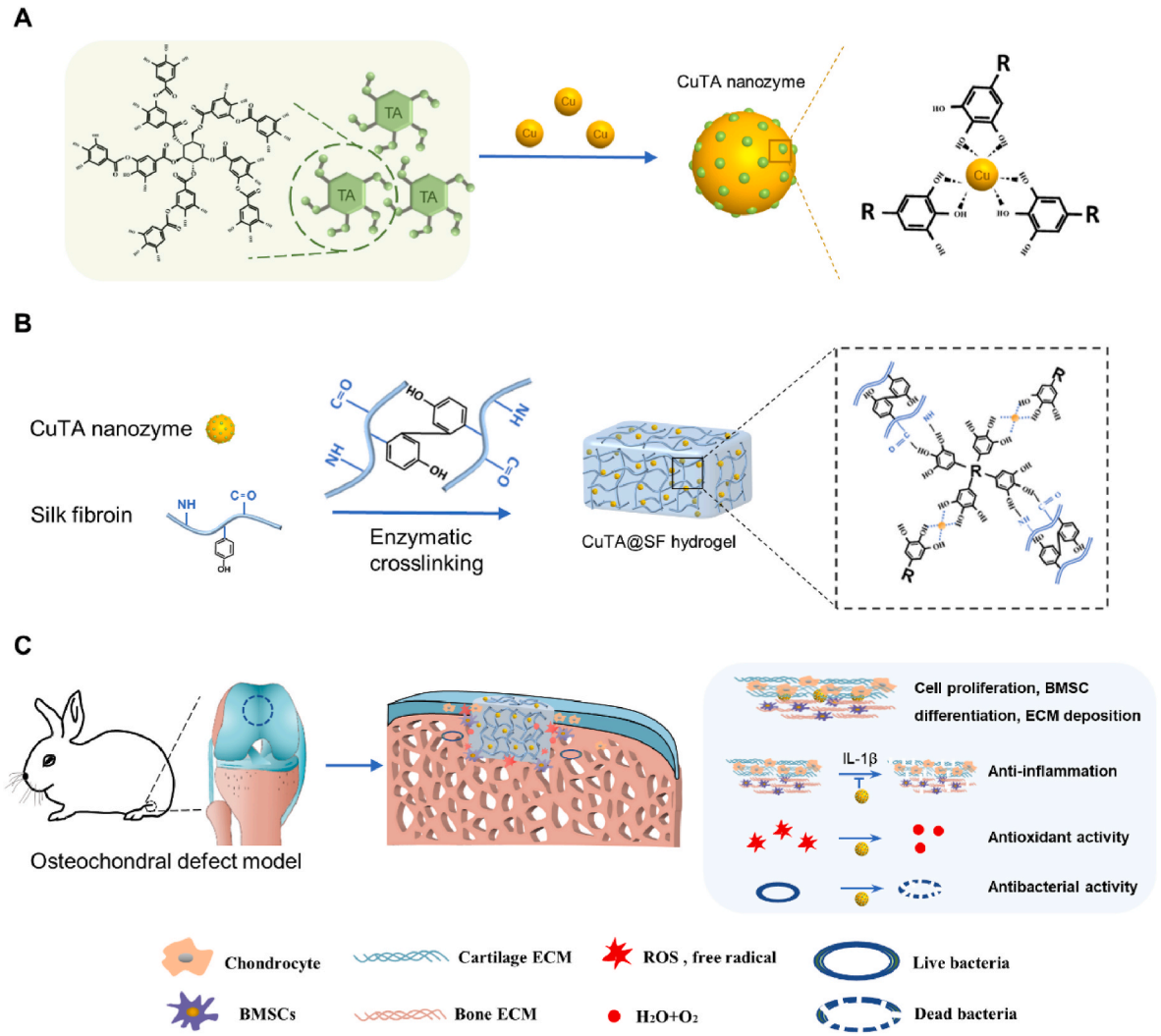

Scheme 1. (A) Schematic illustration of the synthesis of CuTA nanozyme. (B) Schematic illustration of the synthesis of enzymatically crosslinked CuTA@SF hydrogel and the reasonable form of intermolecular connection inside CuTA@SF hydrogel. (C) In the osteochondral defect model of rabbits, the implantation of CuTA@SF hydrogel promoted cell proliferation, BMSC differentiation and ECM deposition. Moreover, CuTA@SF hydrogel had antioxidant, anti-inflammation and antibacterial capacities.

microplate reader (BioTek, USA) at 562 nm wavelength. Thus the content of TA coated on the copper nanoparticles was calculated.

10 mg CuTA nanozyme was incubated in PBS at 37 °C with shaking. At the designed time point, the supernatant was collected and replaced with fresh PBS for each sample. The concentration of TA released was measured with a microplate reader (BioTek, USA) at 562 nm wavelength.

2.4. Scaffold fabrication

Our silk hydrogel was crosslinked through enzyme-catalyzed covalent bonds. 20u/ml horseradish peroxidase (HRP, Sigma-Aldrich) and 0.01% H_2O_2 (Yuanle, Shanghai, China) were added to 4% SF solution and then placed at 37 °C for 1 h to form a transparent SF hydrogel. TA@SF hydrogel contained 50 μg/ml TA and Cu@SF hydrogel contained 64 μg/ml copper nanoparticles. The mixed solution containing CuTA after the reaction of copper nanoparticles and TA was incorporated into the 4% SF solution to acquire CuTA@SF hydrogel.

2.5. pH measurement

The pH of SF, Cu@SF, TA@SF and CuTA@SF was measured with a pH meter (Aquasearcher, OHAUS).

2.6. Scanning electron microscope (SEM) imaging/mapping and transmission electron microscope (TEM)

The hydrogels were freeze-dried for 24 h to receive the test samples. Then samples were sputter-coated with gold and imaged under SEM (Zeiss supra55, Germany) to observe the microstructure of the material surface. Energy dispersive spectrometer (EDS) mapping analysis was conducted on Oxford X-MaxN150 for CuTA@SF hydrogel. The morphology of CuTA was observed with SEM (JEOL JSM-7900F, Japan) and TEM (JEOL JEM-1400Flash, Japan).

2.7. The measurement of pore size and porosity

The pore size of the freeze-dried hydrogels was analyzed with ImageJ software (NIH, USA) using SEM pictures. The porosity was calculated with the ethanol-exchange method [41]. The dried hydrogel was weighed (Wh) and immersed in anhydrous ethanol to get the wet weight (Wa). The porosity of hydrogel was calculated under the following equation: Porosity = Wa- Wh/ρV. ρ represents the density of ethanol, and V is the volume of the dried hydrogel.

2.8. Equilibrium water content

Four groups of hydrogels (1 ml, n = 5) were immersed in PBS for 24 h, and then the resulting gel was lyophilized for 24 h to get a dry gel. The equilibrium water content was calculated by the reduced weight before and after lyophilizing weigh using the following equation. Equilibrium water content = C_w-C_d/C_w, where C_w and C_d refer to the weight of wet and dry hydrogels, respectively.

2.9. Swelling ratio

The swelling ratio of our hydrogel was determined by the weight change at the designed point (0 h, 3 h, 6 h, 12 h, 48 h, 72 h). The hydrogels (1 ml, n = 5) were freeze-dried overnight and then weigh to get the beginning weight (W_b), whereafter the hydrogel was immersed in PBS at 37 °C so that we could obtain the wet weight (W_w), and the swelling ratio was calculated using the following equation: swelling ratio= (W_w - W_b)/W_b

2.10. In vitro degradation

1 ml hydrogel (n = 5) was lyophilized 24 h to get a dry gel (D0), and then the gel was fully immersed in 1 ml PBS placed in a shaker at 37 °C and 100 r. At a designed point, we took out the hydrogel, put it in dH_2O overnight, and placed it in a 37 °C oven to weigh the dry gel (D1)

Weight remains (%) = D_1/ D_0

2.11. SF-TA binding power spectrum analysis and the release of TA from CuTA@SF

We performed fluorometric titration experiments to analyze the binding between SF and TA, as previously reported [42]. 50 μg/ml TA was added to the SF solution and a microplate reader (Thermo Fisher Scientific) was used to record the emission spectra of the mixture from 270 to 550 nm and the excitation wavelength was fixed at 250 nm.

The CuTA@SF hydrogels were immersed in PBS. Then the supernatant was collected and measured with a microplate reader (BioTek, USA) at 562 nm wavelength using the Enhanced BCA Protein Assay Kit (Beyotime, China) to evaluate the release of TA.

2.12. X-ray photoelectron spectroscopy (XPS) analysis

XPS was conducted to analyze the elemental composition of the material surface on the spectrometer (ThermoFisher 250xi).

2.13. Water contact angle

The water contact angle was tested with an optical surface analyzer (OSA100, L10018A302, Lauda Scientific). 5 μl deionized water dropped onto the material's surface, and we recorded the contact angle of water droplets on the surface when they reached a steady state.

2.14. Evaluation of the rheological property

The assessment of the rheological property was performed using a rheometer (Anton Paar, Graz, Austria). Dynamic frequency sweep was performed at 1% strain from 0.1 to 100 rad/s and dynamic strain sweep was carried out from 0.1% to 100% strain at the speed of 10 rad/s. Viscosity was obtained at a shear rate of 0.01–1/s.

2.15. Antioxidant study

(a) DPPH radical-scavenging activity

DPPH working solution containing 250 μM of DPPH (Shanghai Jinsui Bio-Technology, China) in 95% ethanol was prepared. DPPH solution was mixed with our hydrogel. Shaking was then carried in the dark on a shaker under conditions of 200 rpm and 37 °C for 2 h. The absorbance of each reaction solution was detected at 517 nm with a microplate reader (Thermo Fisher Scientific). The DPPH radical-scavenging activity was calculated using the following equation: scavenging efficiency (%) = (A_b - A_r)/A_b Here, A_b is the absorbance value of the blank solution (250 μM DPPH solution) and A_r is the absorbance value of each reaction solution.

(b) Measurement of intracellular ROS

BMSCs and chondrocytes were seeded into a 96-well plate and pretreated with extract of the scaffold from each group for 24 h. 1 ng/ml IL-1β (Genscript, Nanjing, China) or 400 μM H_2O_2 (Yuanle, Shanghai, China) was added to the medium to stimulate cells for 20 min or 24 h, respectively. Then the cells were incubated with a DCFH-DA probe (Beyotime, China) and Hoechst (Beyotime, China) at 37 °C for 20 min. Fluorescence images of each group were obtained using an inverted fluorescence microscope (Mshot, China). Quantification analyses of ROS intensities were done using ImageJ software (NIH, USA). The cells incubated only in the growth medium were treated as NTC and incubated in the medium containing 1 ng/ml IL-1β or 400 μM H_2O_2 were treated as PTC.

2.16. Cell culture

Primary rat BMSCs were purchased from Cyagen Biosciences (Suzhou, China). Mouse chondrocytes were extracted from the joint cartilage tissue of 5 ~ 6-day-old C57Bl/6 mice as previously reported [43]. DMEM low-glucose (Gibco, Carlsbad, CA) with 1% penicillin-streptomycin (P/S, Gibco, Carlsbad, CA) and 10% fetal bovine serum (FBS, Wisent, Canada) was used for cell culture. Cells were incubated in an incubator at 37 °C with 5% CO_2, and the medium was changed every three days.

The extracts SF, Cu@SF, TA@SF, CuTA@SF were prepared as the following steps: 3 ml hydrogel (height: 3 mm, diameter: 3.5 cm) of each group was immersed in 26.6 ml culture medium at 37 °C for 24 h. After removing the hydrogel and filtered with a 0.45 μm filter, the medium was collected and supplemented with FBS and P/S as needed. The harvest medium was stored at 4 °C before use.

2.17. Cell viability

BMSCs and chondrocytes were seeded into a 96-well plate at a density of 10^3 cells/well. The medium was replaced with the test medium when BMSCs were adherent to the wall. After incubated for 48 h, a calcein-AM/PI double staining kit (Dojindo, Japan) was used to measure cell viability. The test medium should be changed with the working solution and incubated in an incubator at 37 °C with 5% CO_2 for 20 min. Then inverted fluorescence microscope (Carl-Zeiss, Germany) was used to observe the cell and collect the images. Quantitative analysis of cell viability was performed using ImageJ software (NIH, USA).

2.18. Cell proliferation

Cell proliferation was measured with the CCK8 kit (APExBIO, USA) following the producers' suggestions. Briefly, cells were cultured in 96 well plates for 1, 3, 5 days with a primary density of 10^3 cells/well. At the designed point, the test medium was replaced by a 10% CCK8 working solution and was incubated in an incubator at 37 °C with 5% CO2 for 1 h. The absorbance of the culture medium was measured at 450 nm wavelength employing a microplate reader (BioTek, USA).

2.19. Osteogenic differentiation

(a) BMSCs were cultured in 96-well plates with a growth medium (DMEM, 10% FBS, 1% P/S). After adherent to the well, the medium was replaced with an osteogenic induction medium containing 10% FBS, 1% P/S, 10^{-5} M β-glycerophosphate (Gibco, Carlsbad, CA), 10^{-5} M dexamethasone (Sigma, St. Louis, MO), 50 mg L^{-1} l-ascorbic acid (Sigma, St. Louis, MO). The medium was changed every three days until seven days. The BCIP/NBT Alkaline Phosphatase Color Development Kit (Beyotime, China) was used following the producers' suggestions to evaluate the positive induction of osteogenesis. The samples were further stained with DAPI (Beyotime, China) to calculate the positive-stained cell number. The image analysis was performed in ImageJ software (NIH, USA).
(b) 1 ng/ml IL-1β was added into the test medium, and the rest of the procedure was followed as above to assess the ability of the test medium against the effect of proinflammatory cytokine on osteogenesis. The BMSCs incubated only in the osteogenic medium were treated as NTC and incubated in osteogenic differentiation medium with 1 ng/ml IL-1β stimulated was treated as PTC.

2.20. The deposition of glycosaminoglycan (GAG) in the cartilage ECM

(a) Chondrocytes were cultured in 96-well plates with a growth medium (DMEM, 10% FBS, 1% P/S). After adherent to the well, the medium was replaced with L-DMEM containing the extract of hydrogels. Alcian blue staining (1%, pH = 2.5, Macklin, China) was used to assess the level of GAG in the ECM of chondrocytes. Staining was eluted with 6 M guanidine hydrochloride (Sinopharm, China), the final dye solution was detected at 630 wavelengths with a microplate reader.
(b) 1 ng/ml IL-1β was added into the medium containing the extract of hydrogels, and the rest of the procedure was followed as above to assess the ability of hydrogel against the effect of proinflammatory cytokine on ECM degradation. The chondrocytes incubated only in growth medium were treated as NTC and incubated in L-DMEM combined with 1 ng/ml IL-1β were treated as PTC.

2.21. Antibacterial activity

In this study, *Staphylococcus aureus* was employed to evaluate our hydrogel's antibacterial ability, which is the most common pathogen of surgical infections. 100 μl bacterial suspension at a concentration of 3.75×10^9 CFU/ml was added to a 10 cm dish prepared with agar medium. After incubated for 24 h, the bacteria Petri dish was taken out to measure the antibacterial ring's diameter to evaluate the antibacterial properties of the gels.

The microplate proliferation assay was conducted to evaluate the in vitro antimicrobial activity of CuTA@SF as previously reported [44,45]. Hydrogels were incubated with 500 μl bacterial suspension at a concentration of 10^7 CFU/ml in the 48-well plate at 37 °C for 1 h. Then 200 μl of the resulting soluting was transferred to a new 96-well plate. Proliferation over 12 h was observed with a microplate reader (BioTek, USA) at 630 nm wavelength.

2.22. Western blot (WB)

WB was conducted to evaluate the protein expression level after culturing BMSCs and chondrocytes with hydrogels for 7days or 5 days. The protein of the cells was extracted with a Total ProteoExtract Kit (KeyGEN, Nanjing, China). After measuring the concentration with a BCA Protein Assay Kit (KeyGEN, Nanjing, China), the proteins were separated with SDS-PAGE electrophoresis and transferred to PVDF membranes. Blocking with 5% BSA for 1 h, the PVDF membranes were incubated with the primary antibodies at 4 °C. The antibodies applied include anti-SOX-9 (Proteinteck, China), anti-COL-2 (Abcam, UK), anti-RUNX2 (Proteinteck, China), anti-COL I (Proteinteck, China), GAPDH (KeyGEN, Nanjing, China). After washing in Tris buffered saline–Tween (TBST), the blots were developed with an HRP-conjugated secondary antibody and visualized with ChemiDoc MP Imaging System (Bio-rad). Protein band intensity was quantified using ImageJ and normalized to the corresponding GAPDH bands (NIH, USA).

2.23. Proteomics analysis

BMSCs were cultured with an osteogenic induction medium containing the extract of SF and CuTA@SF hydrogels exposed to 1 ng/ml IL-1β for 7 days. Chondrocytes were cultured with L-DMEM containing the extract of SF and CuTA@SF exposed to 1 ng/ml IL-1β for 5 days. At the designed time point, samples (n = 3/group) were collected to extract protein for further reverse-phase high-performance liquid chromatography (RP-HPLC). The result of mass spectra underwent qualitative and quantitative analysis on MaxQuant/Andromeda software (version 1.3.0.5). Further data analysis was conducted on DAVID, String, Cytoscape and OmicStudio (OmicStudio tools at https://www.omicstudio.cn/tool). Differentially expressed proteins were defined as $P < 0.05$. The proteomics data were deposited in the iProX database (https://www.iprox.cn/, protein ID: IPX0004122000).

2.24. Animal model

The ethical inspection committee of the Nanjing first hospital approved the study protocol. Fifteen New Zealand white rabbits were used in this study. We prepared the hydrogels and preserved them in a wet environment before surgery. After general anesthesia, OCD surgery (height: 4 mm, diameter:5 mm) was performed on the femoral condyle to implant the four pre-formed hydrogels (SF, Cu@SF, TA@SF, CuTA@SF). The defect region had no treatment designed as a control (CTL), and every group had six parallel samples. All rabbits received the intramuscular injection of the antibiotic drug for three days. After 12-week post-operation, all animals were sacrificed, and the femur condyle was collected for further study.

2.25. Macroscopic and histological assessment

Firstly, the samples were observed with a stereoscope. Paraformaldehyde was used to fix tissue and samples were immersed in EDTA at 37 °C for one month to decalcify. After being embedded in paraffin and sliced, the sections were stained with hematoxylin-eosin (HE), safranin O/fast green (S/O), and toluidine blue staining to determine the type of the neo-tissue. Immunohistochemistry was used to specifically analyze the expression of type I collagen (COL I) and proteoglycan (AGG) in the osteochondral region. According to the established histological scoring system, we conducted cartilage and subchondral bone evaluation [46].

2.26. Micro-CT evaluation

The knee samples were scanned and imaged with a micro-CT scanner (SkyScan1176, Bruker, Germany). The Source Voltage and Source Current of the scanning were 70 kV and 329μA. The obtained image under the resolution of 9 μm was analyzed with CTan (Bruker, Germany) to get data including bone mineral density (BMD), bone volume/total volume (BV/TV), trabecular thickness (Tb. Th) and trabecular numbers (Tb. N). Then the 3D reconstruction was performed with the software DataViewer (Bruker, Germany) and CTvox (Bruker, Germany).

2.27. Total RNA isolation and quantitative real-time reverse transcriptase-polymerase chain reaction (qRT-PCR)

BMSCs and chondrocytes were cultured with the test medium for 5 or 7 days. Total RNA extraction was performed using an RNA prep Pure Cell/Bacteria Kit (Tiangen, China), following the product's instructions. Then the concentration of RNA was measured and reverse transcriptase was performed to get cDNA. qRT-PCR was conducted with an SYBR Green qPCR Kit (Accurate Biotechnology Co., Ltd., China). Primer sequence of target genes (Genscript, China) are:

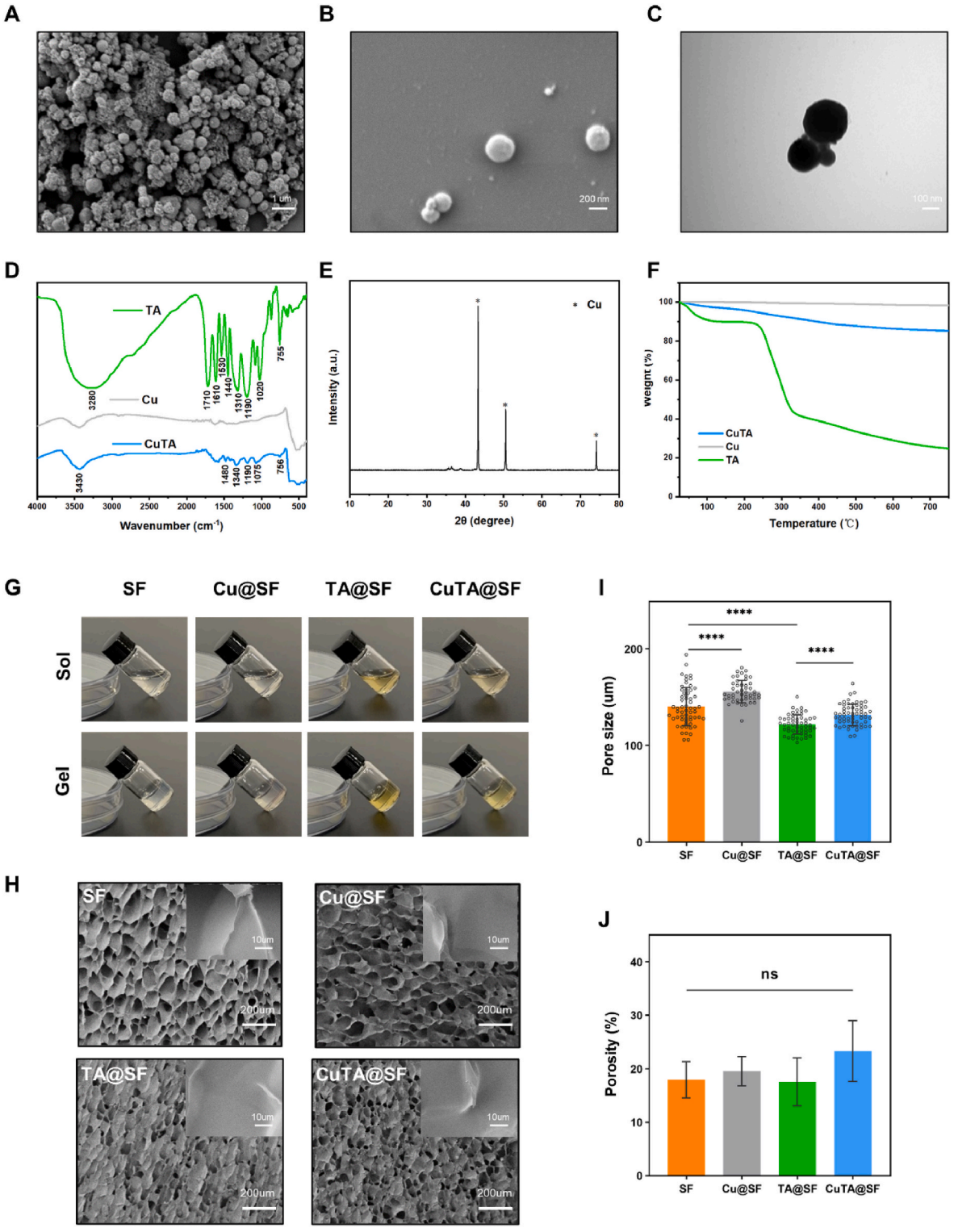

Fig. 1. (A–B) SEM image of CuTA nanozyme. (C) TEM image of CuTA nanozyme. (D) FTIR of CuTA, Cu and TA. (E) XRD of CuTA. (F) Thermogravimetry analysis of CuTA, Cu and TA. (G) Transition before and after gelation of SF, Cu@SF, TA@SF, CuTA@SF hydrogels. (H) Microstructure of lyophilized SF, Cu@SF, TA@SF, CuTA@SF hydrogels from SEM images. (I) The pore size of SF, Cu@SF, TA@SF, CuTA@SF hydrogels was quantified from SEM images with ImageJ. (J) The porosity of SF, Cu@SF, TA@SF, CuTA@SF hydrogels. Results were shown as mean ± SD, ****$p < 0.0001$.

Target gene	species	forward	reverse
GAPDH	Rat/Mouse	GCAAGTTCAACGGCACAG	CGCCAGTAGACTCCACGAC
COL I	Rat	TGGATGGCTGCACGAGT	TTGGGATGGAGGGAGTTTA
RUNX2	Rat	CCAACTTCCTGTGCTCCGTG	GTGAAACTCTTGCCTCGTCCG
COL-2	Mouse	CCTCCGTCTACTGTCCACTGA	ATTGGAGCCCTGGATGAGCA
SOX-9	Mouse	CGGCTCCAGCAAGAACAAG	GCGCCCACACCATGAAG
ADAMTS5	Mouse	GCCATTGTAATAACCCTGCACC	TCAGTCCCATCCGTAACCTTTG
NRF2	Mouse	TAGATGACCATGAGTCGCTTGC	GCCAAACTTGCTCCATGTCC
SOD-1	Mouse	AACCAGTTGTGTTGTCAGGAC	CCACCATGTTTCTTAGAGTGAGG
HO-1	Mouse	GATAGAGCGCAACAAGCAGAA	CAGTGAGGCCCATACCAGAAG

2.28. Statistics

Statistical analysis was conducted using one-way ANOVA with Tukey's multiple comparisons and comparisons between 2 groups were evaluated by *t*-test. All data were expressed as means ± standard deviation (SD). Differences were considered statistically significant when $p < 0.05$.

3. Result and discussion

3.1. Fabrication and characterization of CuTA@SF hydrogel

CuTA nanozyme was fabricated by modifying copper nanoparticles with TA to form a CuTA coordination framework (Scheme 1A), and its nano-structure was revealed by the SEM and TEM images with an average diameter of 470.42 ± 140.21 nm (Fig. 1A–C). Quantitative results showed that the particle size of copper nanoparticles (440.00 ± 124.26 nm) had no significant difference compared with that of CuTA nanozyme (Figs. S1A and B). We further used BCA assays to determine the amount of TA coated on the surface of copper nanoparticles. 18.19% TA i.e., 1.819 mg was firmly coated on copper nanoparticles when immersed in 10 mg TA solution for 24 h. From the FTIR spectrum of TA (Fig. 1D), the broad absorption peak at 3280 cm^{-1} was –OH vibration and C═O stretching vibration appeared at 1710 cm^{-1}. The absorption peaks at 1610 cm^{-1}, 1530 cm^{-1} and 1440 cm^{-1} represented benzene ring skeleton and C═C vibration. C–H stretching vibration appeared at 1310 cm^{-1}. 1190 cm^{-1} and 1020 cm^{-1} were the vibrations of C–O–C. 755 cm^{-1} was the vibration peak of the C–H on the side chain benzene ring. The above characteristic absorption peaks were consistent with the characteristic structure of TA [47–50]. TA could be adsorbed on the surface of nanoparticles, possibly by interaction with π electrons and carbonyl groups as previously reported [27,51,52]. In the spectrum of CuTA (Fig. 1D), we could find some notable absorption peaks in contrast to original copper nanoparticles including at 1480 cm^{-1}, 1340 cm^{-1}, 1190 cm^{-1}, 1075 cm^{-1} and 756 cm^{-1}, which are the characteristic absorption peak of TA, indicating the interaction between the copper nanoparticles and the benzene ring, C–H, C–O–C of TA. Therefore, copper nanoparticles were successfully modified with TA to form CuTA nanozyme. The XRD pattern of CuTA nanozyme showed sharp peaks at diffraction angles 43.3°, 50.55° and 74.29°, which are the characteristic diffraction angles of copper [53] (Fig. 1E). The thermal stability of the CuTA nanoparticles was higher than TA and lower than the original copper nanoparticles shown in TG curves (Fig. 1F). 10 mg CuTA nanozyme was further immersed in PBS solution to evaluate the release of TA. About 0.51 mg of the TA was released on the first day. The release curves displayed about 0.96 mg of the TA release into the PBS solution after 6 days of incubation (Fig. S2). The prepared CuTA nanozyme was subsequently incorporated into SF solution, followed by enzymatic crosslinked via HRP and H_2O_2 to form a stable CuTA@SF hydrogel (Scheme 1B). HRP and H_2O_2 were adopted to promote crosslinking of tyrosine residues of SF, leading to a transparent appearance and stable structure of hydrogel [54]. The transition before and after gelation was shown in Fig. 1G and the pure silk hydrogel was clear and transparent. The color of SF hydrogel turned brown and yellow with the incorporation of copper nanoparticles, TA or CuTA nanozyme. It has been reported that the residual H_2O_2 content in the enzymatically crosslinked SF hydrogel was quite low and non-toxic [55], implicating that our hydrogels will not cause additional oxidative stress after being implanted to the injury site.

Pore size and porosity are critical criteria in the design of scaffold. Proper pore size and porosity can provide a favorable microenvironment for the migration and proliferation of cells without reducing the mechanical properties of the scaffold [56,57]. Scanning electron microscopy (SEM) was used to observe the microstructure of the hydrogel. It was observed that the pore morphology was changed with the incorporation of copper nanoparticles, TA or CuTA nanozyme (Fig. 1H). Cu@SF had the largest pore size (156.1 ± 11.44 μm) compared with the other three groups. The existence of copper nanoparticles might affect the structure of silk fibroin causing larger porous structures. The same phenomenon was reported in previous research where Villanueva et al. found that the starch hydrogel incorporated with copper nanoparticles displayed an increased pore size [58]. While with the addition of TA, the pore size of TA@SF became smaller (122.0 ± 10.05 μm, $p < 0.0001$) compared with that of SF (140.4 ± 19.66 μm, Fig. 1I). The formation of hydrogen bonds between SF and TA resulted in the smaller pore size and uniform structure of TA@SF. The pore size of the CuTA@SF hydrogel (131.9 ± 11.10 μm) was not significantly reduced as compared with that of SF hydrogel (Fig. 1I). The porosity of CuTA@SF (23.34 ± 5.70%) was higher than that of other hydrogels such as SF (17.95 ± 3.40%), Cu@SF (19.56 ± 2.73%) and TA@SF (17.56 ± 4.49%), although there was no statistically significant difference between groups (Fig. 1J). It has been observed in previous studies that the pore size of scaffold with a diameter of 100–160 μm was beneficial for the regeneration of cartilage and bone [59–61]. Hence, our silk-based hydrogels are suitable for the repair of OCD.

The elemental mapping verified that the copper element was successfully located on the surface of CuTA@SF hydrogel (Fig. 2A). The existence of copper nanoparticles was further confirmed by XPS, and the copper content of the CuTA@SF and Cu@SF was 0.21% and 0.19%, respectively (Fig. 2B). The difference in the content of C, N, O between Cu@SF and CuTA@SF was negligible. To observe the interaction between SF and TA, we performed fluorometric titration experiments [42]. In the fluorescence emission spectra, the wave peak of 1% and 4% SF solution was located at 305 nm. And the intensity at 305 nm was significantly decreased with the incorporation of 50 μg/ml TA, confirming the formation of the chemical bond between SF and TA in the hydrogel (Fig. S3). The BCA assay was also used to measure the release of TA from CuTA@SF. After incubation in PBS for 3day, the release of TA (15.94 ± 0.72 μg, 31.89 ± 1.44%) reached a steady state (Fig. S4). The pH value of the hydrogel solutions showed no significant difference between the groups: SF (6.21 ± 0.04), Cu@SF (6.21 ± 0.05), TA@SF (6.18 ± 0.04), CuTA@SF (6.24 ± 0.05) (Fig. S5).

TA, a widely-used natural surface modifier, could improve the hydrophilicity of base materials like sodium alginate, polycaprolactone and polyvinylidene [25,28,62]. Therefore, we compared the hydrophilicity of the prepared hydrogels through water contact angle and equilibrium water content. CuTA@SF and TA@SF exhibited a smaller water contact angle at 5° and 18° compared with SF (40°) and Cu@SF (27°),

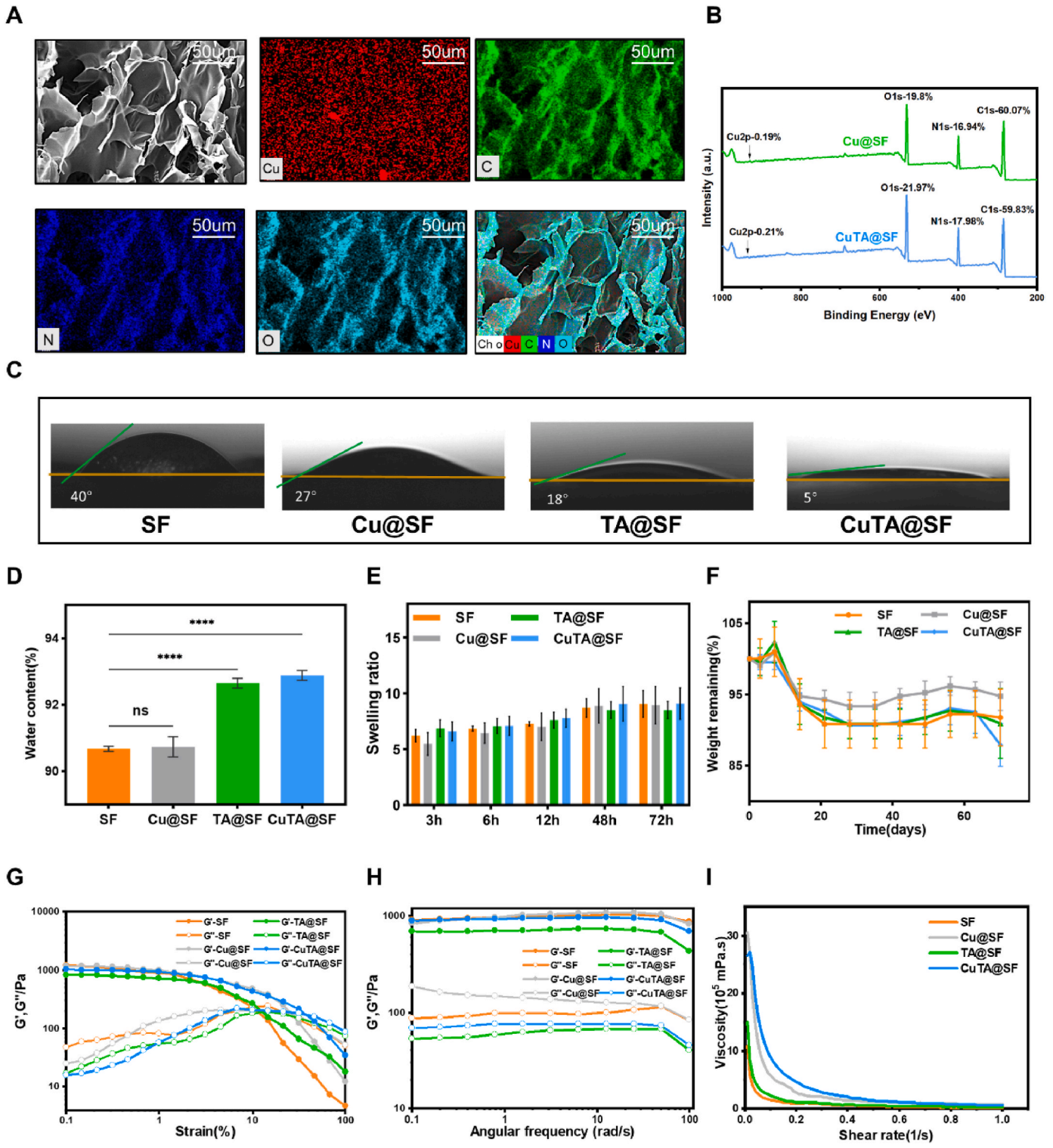

Fig. 2. (A) The EDS-mapping analysis of CuTA@SF hydrogel. (B) Surface elemental analysis of Cu@SF and CuTA@SF hydrogels with XPS. (C) The water contact angle of SF, Cu@SF, TA@SF and CuTA@SF hydrogels using deionized water. (D) The Equilibrium water content of SF, Cu@SF, TA@SF and CuTA@SF hydrogels. (E) The swelling ratio of SF, Cu@SF, TA@SF and CuTA@SF hydrogels in PBS at 37 °C. (F) In vitro degradation curves of SF, Cu@SF, TA@SF and CuTA@SF hydrogels in PBS at 37 °C. (G) Dynamic modulus of SF, Cu@SF, TA@SF and CuTA@SF hydrogels at varying stains from 0.1% to 100%. (H) Dynamic modulus of SF, Cu@SF, TA@SF and CuTA@SF hydrogels at varying angular frequency from 0.1 to 100 rad/s. (I) Viscosity-shear rate curves of SF, Cu@SF, TA@SF and CuTA@SF hydrogels. Results were shown as mean ± SD, ****$p < 0.0001$.

which indicated the better hydrophilic properties of the material surface as the addition of TA (Fig. 2C). The equilibrium water content of TA@SF (92.65 ± 0.147%, $p < 0.0001$) and CuTA@SF (92.89 ± 0.148%, $p < 0.0001$) were also increased compared with SF (90.68 ± 0.074%), implying that TA@SF and CuTA@SF could absorb more water under the equal condition (Fig. 2D). The better hydrophilic property indicated that TA@SF and CuTA@SF could absorb more nutrition in the communication with the surrounding liquid environment and recruit more BMSCs

following the infiltration of bone marrow blood [63,64].

The swelling ratio results demonstrated that all hydrogels reached a swelling equilibrium state after 72 h, with no obvious difference between groups at 3 h, 6 h, 12 h, 48 h and 72 h (Fig. 2E). Next, we observed the degradation of hydrogels in the PBS solution. The CuTA@SF hydrogel underwent continuous degradation with 87.9% remaining at 70 days (Fig. 2F). Concretely, the stability of the hydrogels ensures the early support for tissue regeneration, while the slow degradation of the hydrogels could give space for the growth of neo-tissues [65,66]. The SF hydrogel before and after degradation were examined with FTIR analysis to detect the change in secondary structure. From the FTIR spectra of SF hydrogel before degradation, the C–N stretching at 1234 cm^{-1} remained unchanged. The C═O stretching at 1634 cm^{-1} was shifted to 1625 cm^{-1} and the N–H bending at 1514 cm^{-1} was shifted to 1527 cm^{-1}, which were attributable to the formation of β-sheet structure [67] (Fig. S6). Moreover, the characteristic structure induced by the β-sheet structure cannot be clearly detected in the FTIR spectra of SF hydrogel after degradation, indicating the destruction of the secondary structure. However, the degradation of the hydrogel in PBS in vitro cannot fully imitate its degradation in vivo. Further precise degradation systems, such as enzymatic degradation, are needed to simulate the degradation process in vivo.

Then we conducted the rheological experiment to evaluate the flow and deformation of the prepared hydrogel under external force. From the strain sweeps, the incorporation of TA, copper nanoparticles or CuTA nanozyme did not change the linear-viscoelastic (LVE) region (Fig. 2G). The storage modulus (G′) at 0.1–100 rad/s of SF, Cu@SF, TA@SF and CuTA@SF were higher than the loss modulus (G″), indicating the stable mechanical strength of hydrogels (Fig. 2H). Previous studies confirmed that adding copper into base materials like bioceramic and alloy would achieve elevated mechanical properties [68,69]. However, the addition of 64 μg/ml copper nanoparticles did not significantly change the mechanical properties of the SF hydrogel in this current study. One reasonable explanation is that the amount of copper nanoparticles we used was relatively low to enhance the crosslinking of the hydrogel. The incorporation of TA could not enhance the mechanical properties of hydrogels from the result of the rheological experiment (Fig. 2G and H). However, previous studies have reported the improved mechanical properties of scaffold as the incorporation of TA [23,70]. Unlike those studies using TA as a cross-linking agent, the crosslinking of our hydrogel was mediated by HRP/H_2O_2 system and TA is mainly acting as a bioactive molecule. The viscosity-shear rate curve showed that CuTA@SF, TA@SF and Cu@SF had higher viscosity values compared with SF (Fig. 2I). TA contains a high density of polyphenol groups, which allows it to interact with other molecules via hydrogen bonding and display significant surface adhesion [71]. Metal nanoparticles such as copper and silver might participate in the dense crosslinking network of hydrogel [58,72], resulting in increased viscosity. When implanted into the defect area, enhanced viscosity would facilitate the connection between the hydrogel and surrounding tissues [73,74].

Through the above experiments, we have demonstrated the successful fabrication of CuTA@SF hydrogel and revealed the different physicochemical properties of SF, Cu@SF, TA@SF and CuTA@SF hydrogels.

3.2. The cytocompatibility and antibacterial activity of CuTA@SF hydrogel

In order to evaluate the cytocompatibility of CuTA@SF hydrogel, we first performed live/dead staining assay. BMSCs and chondrocytes were incubated in a growth medium containing the extract of hydrogels for 3 days. The viability of BMSCs reached over 90% in Cu@SF, TA@SF and CuTA@SF, which was significantly higher than that of SF hydrogel (Fig. 3A and B). In the group of chondrocytes, TA@SF (90.78 ± 4.34%), Cu@SF (93.66 ± 3.97%) and CuTA@SF (96.07 ± 1.87%) also showed higher cell viability compared with SF (85.97 ± 4.54%), implying enhanced cytocompatibility as the incorporation of TA, copper nanoparticles or CuTA nanoparticles (Fig. 3D and E).

The proliferation of cells over time was evaluated by CCK8 assay. The results of BMSCs showed that cells cultivated in Cu@SF, TA@SF and CuTA@SF grew significantly faster at day 1 compared with SF. Besides, Cu@SF and CuTA@SF had higher proliferation rates compared with SF and TA@SF on day 3 and 5 (Fig. 3C). As for chondrocytes, it was observed that TA@SF significantly promoted cell proliferation at day 1 compared with SF and Cu@SF. Compared with SF, the functionalized hydrogels (Cu@SF, TA@SF and CuTA@SF) showed no promoting effect on cell proliferation on day 3 but had a significant pro-proliferation ability on day 5 (Fig. 3F). Consequently, the incorporation of copper or CuTA nanoparticles significantly increased the proliferation of BMSCs and chondrocytes. Consistent with previous research [75], as copper is a cofactor for many critical metabolic enzymes in the body and encourages the release of essential growth factors like IGF [76], copper-containing material possessed pro-proliferation capacity. Besides, TA can promote the proliferation of chondrocytes at an early stage, which was possibly caused by the polyphenol structure covalently interacting with the ECM of chondrocytes [77]. In conclusion, the incorporation of 50 μg/ml TA and 64 μg/ml nano-copper into SF-based biomaterial was safe enough for OCD regeneration. And CuTA@SF significantly accelerated the proliferation of BMSCs and chondrocytes.

Infections often lead to delayed healing of bone defects and surgery failure, which is a major obstacle to the application of orthopedic implants. Especially for implants in the joint cavity, once infection occurs it will cause irreparable damage to the function of the entire joint, and revision surgery is needed ultimately. The antibacterial activity of copper nanoparticles was associated with membrane damage, plasmid DNA degradation and oxidative stress in a dose-dependent manner [78]. TA was applied to antibacterial material increasingly due to the rich galloyl group [30,79]. Since TA and copper are well-known antibacterial molecules, the antibacterial ability of CuTA@SF hydrogels was evaluated with *Staphylococcus aureus*, one of the most common bacteria in surgical infections. In the agar diffusion experiment, CuTA@SF exhibited the largest diameter of the antibacterial ring (16.50 ± 2.29 mm, $p < 0.05$ for CuTA@SF vs SF, Fig. 3G and H). TA@SF and Cu@SF also exhibited antibacterial activity compared with SF in the gross view of the antibacterial ring, but there was no statistically significant difference between these three groups (Fig. 3G and H). As antibacterial activity is positively correlated with the concentration of antibacterial molecules, the concentration of TA and copper nanoparticles in this study was not enough to show an antibacterial effect alone in the agar diffusion experiment. The microplate proliferation assay was further carried out to evaluate the antibacterial activities of hydrogels for 12 h. The results indicated that *Staphylococcus aureus* grew slowly incubated with Cu@SF, TA@SF and CuTA@SF hydrogels compared with SF hydrogels. CuTA@SF displayed the best capacity to suppress bacterial growth for 12 h (Fig. 3I). Hence, CuTA@SF is a suitable candidate to eliminate pathogenic microorganisms that may exist in the microenvironment after OCD.

3.3. Effect of CuTA@SF hydrogel on BMSCs differentiation and deposition of cartilage ECM

After confirming that the developed hydrogels have favorable cytocompatibility, we next evaluated their capacity to influence BMSCs differentiation. Alkaline phosphatase (ALP) is an important indicator for early bone formation and we conducted ALP staining for BMSCs culturing with the induction medium containing the extract of hydrogels for 7 days. BMSCs treated with CuTA@SF had the highest staining intensity and area compared with the other three groups (Fig. 3J). Further quantitative analysis showed that CuTA@SF enhanced the staining intensity and possessed the most positive-stained cells compared with other groups (Fig. 3K and L). Cu@SF and TA@SF did not alter the

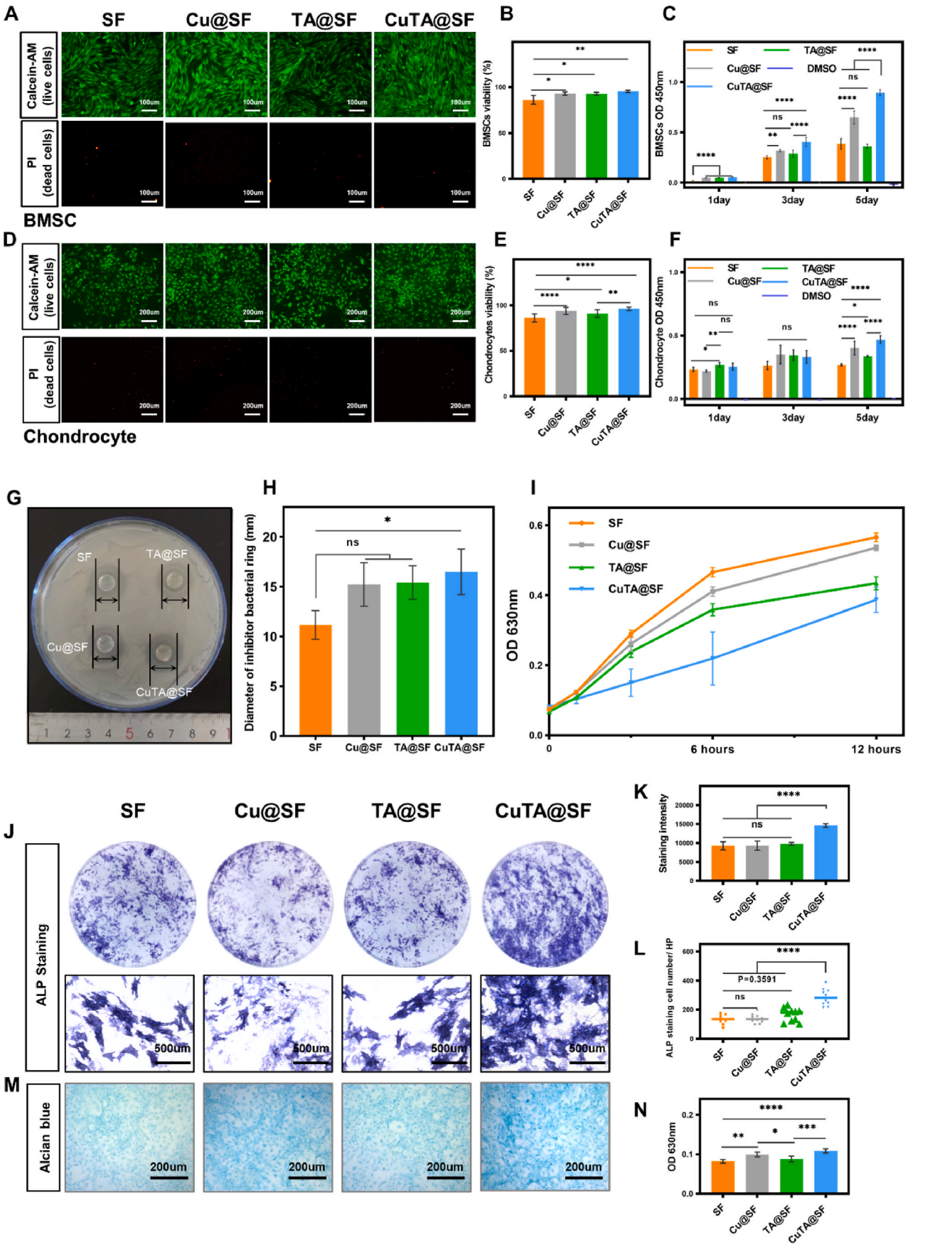

(caption on next page)

Fig. 3. (A) Cell viability of BMSCs cultured in the extract of SF, Cu@SF, TA@SF and CuTA@SF hydrogels was evaluated with Live/dead staining. (B) Quantification of BMSCs viability with the image of Live/dead staining. (C) The proliferation of BMSCs cultured in the extract of SF, Cu@SF, TA@SF and CuTA@SF hydrogels at 1,3,5 days was evaluated with CCK-8. (D) Cell viability of chondrocytes cultured in the extract of SF, Cu@SF, TA@SF and CuTA@SF hydrogels was evaluated with Live/dead staining. (E) Quantification of chondrocytes viability with the image of Live/dead staining. (F) The proliferation of chondrocytes cultured in the extract of SF, Cu@SF and CuTA@SF hydrogels at 1,3,5 days was evaluated with CCK-8. (G) The image of SF, Cu@SF, TA@SF and CuTA@SF hydrogels were placed on the agar medium containing *Staphylococcus aureus*. (H) The anti-bactericidal activity of SF, Cu@SF, TA@SF and CuTA@SF hydrogels were evaluated with the inhibition halo diameters against *Staphylococcus aureus*. (I) The antibacterial activity of SF, Cu@SF, TA@SF and CuTA@SF hydrogel was evaluated by microplate proliferation assay. (J) Stereoscope and microscopic images of BMSCs co-stained with ALP and DAPI. (K) Quantification of ALP staining with stereoscope images. (L) The number of ALP positive-stained cells. (M) Alcian blue staining for chondrocytes cultured in the extract of SF, Cu@SF, TA@SF and CuTA@SF hydrogels. (N) Quantification of Alcian blue staining. Results were shown as mean ± SD, *$p < 0.05$, **$p < 0.01$, ***$p < 0.001$, ****$p < 0.0001$.

staining intensity and positive-stained cell number compared with SF, indicating the addition of copper nanoparticles and TA alone could not facilitate the production of ALP on day 7 (Fig. 3K and L). BMSCs differentiate into specific lineages following the early activation of BMSCs to the defect site, which is critical to OCD regeneration. Copper could stimulate the differentiation of mesenchymal stem cells into osteoblasts and improve the biological process essential for endothelial cell proliferation by upregulating the expression of vascular endothelial growth factor (VEGF) [80–82]. TA was frequently employed as a particularly ideal coating to reinforce the bone-implant interface due to its microenvironment improved capabilities [83,84]. The combination of copper nanoparticles and TA would achieve a better performance in the osteogenesis of BMSCs, which implied that the novel CuTA@SF hydrogel had the potential to promote the osteogenic differentiation of BMSCs.

The content of GAG produced by chondrocyte was evaluated by Alcian blue staining after 3-day culturing. The staining intensity of CuTA@SF and Cu@SF was stronger than that of the TA@SF and SF as shown in Figure 3M. Subsequent quantitative analysis at 630 nm wavelength confirmed that the staining intensity of CuTA@SF and Cu@SF was significantly higher than that of SF and TA@SF, indicating that copper-containing hydrogels increased the GAG production from chondrocytes. CuTA@SF had the highest content of GAG compared with SF, Cu@SF and TA@SF, accelerating the deposition of GAG (Figure 3N). Previous studies have established that copper was essential for the homeostasis of cartilage ECM through GAG deposition and copper-dependent enzyme lysyl oxidase-mediated collagen cross-linking [85–87]. Hence, CuTA@SF hydrogel is a potential biomaterial for cartilage injury healing.

3.4. The antioxidant activity of CuTA@SF hydrogel

The in vitro antioxidant activity of CuTA@SF hydrogels was evaluated by DPPH radical scavenging experiment. DPPH solution shows a deep purple color with active free radicals and the color will turn yellow when antioxidants exist. As shown in Fig. 4A, the DPPH solution containing SF and Cu@SF hydrogels still exhibited deep purple. However, the solution turned yellow in the group of TA@SF and CuTA@SF. Further quantitative analysis at 517 nm wavelength showed that the DPPH elimination rate of TA@SF and CuTA@SF both reached 60%, significantly higher than that of SF (10.9%) and Cu@SF (10.8%) (Fig. 4B), indicating that TA or CuTA nanozyme can efficiently scavenge DPPH while copper nanoparticles alone did not possess in vitro antioxidant ability.

Due to the tight connection between ROS and inflammatory factors, we tried to detect the intracellular ROS level of BMSCs and chondrocytes after being stimulated with inflammatory factors, IL-1β. Fluorescent staining showed an elevated level of intracellular ROS in the simulated inflammatory environment of PTC compared with NTC (Fig. 4C). The ROS fluorescence intensity of the BMSCs and chondrocytes pretreated with the extract of Cu@SF, TA@SF and CuTA@SF was significantly decreased compared with that of SF (Fig. 4C, E, F). Cu@SF exhibited excellent performance in scavenging intracellular ROS different from the DPPH experiment. As copper nanoparticles cannot directly react with ROS in vitro shown in the DPPH experiment, we speculated that the release of copper may strengthen the activity of antioxidant enzymes in the cells to modulate oxidative stress, and this function can only be reflected in living cells.

H_2O_2, a stable form of ROS, can promote the generation of intracellular ROS [88]. To further verify the antioxidant activity of CuTA@SF hydrogel, BMSCs and chondrocytes were treated with H_2O_2 containing the extract of SF, Cu@SF, TA @SF and CuTA@SF hydrogels for 24 h. The strong green fluorescence could be observed in BMSCs and chondrocytes after H_2O_2 was treated (Fig. 4D). The Cu@SF, TA@SF and CuTA@SF groups showed negligible green fluorescence compared with SF (Fig. 4D, G, H), indicating that Cu@SF, TA@SF and CuTA@SF could effectively scavenge intracellular ROS upon H_2O_2 stimulation.

Overall, copper nanoparticles, TA and CuTA nanozyme played their respective roles in scavenging ROS. The application of CuTA@SF could efficiently resist oxidative stress not only by directly reacting with ROS such as DPPH and H_2O_2 but also by regulating inherent antioxidant capacity.

3.5. The activity of modulating the local inflammatory environment

The initiation of acute inflammation would trigger a healing cascade which may act as a pro-repair factor when an osteochondral defect occurs. However, chronic inflammation would develop if the homeostasis of inflammation and anti-inflammation was not maintained well [89,90]. It is crucial to fabricate a material that could modulate the local inflammatory environment and promote the regeneration progress at the same time [91], especially in critical size osteochondral defects in which the spontaneous regeneration capacity is insufficient. The overexpression and release of inflammatory factors in the local microenvironment after injury, such as IL-1β, hinder the differentiation of MSCs and accelerate the degradation of the ECM. In our study, we used 1 ng/ml IL-1β to simulate the local environment in the joint after OCD. BMSCs were incubated in an osteogenic medium containing extract of hydrogels and simultaneously exposed to 1 ng/ml IL-1β. The degree of osteogenesis was evaluated by ALP staining after 7 days of induction. The results demonstrated that ALP staining intensity was obviously decreased after being stimulated with IL-1β, implying that inflammatory factors inhibited the early osteogenic differentiation of BMSCs (Fig. 5A). SF, Cu@SF and TA@SF presented the weakened ALP staining compared with NTC, indicating the poor ability of these hydrogels against IL-1β that impede osteogenesis (Fig. 5A, C). However, the ALP staining intensity of CuTA@SF reached the level of NTC, demonstrating that the incorporation of CuTA nanozyme significantly alleviated the microenvironment that inhibited osteogenesis under the existence of inflammatory factors (Fig. 5A, C). Although the ALP staining intensity was not significantly improved, CuTA@SF enhanced the ALP positive-stained cell number as compared with that of PTC. Besides, CuTA@SF had the highest ALP positive-stained cell number compared with SF, Cu@SF and TA@SF (Fig. 5D). Therefore, CuTA@SF could reverse the inhibitory effect of IL-1β on BMSC osteogenesis.

The expression levels of osteogenic genes *COL I* and *RUNX2* were evaluated with q-PCR under the same treatment. The CuTA@SF showed a higher gene expression of *COL I* (2.4-fold, $p < 0.0001$) at day 7 compared with PTC. The Cu@SF and TA@SF also exhibited higher expression levels of *COL I* about 1.91-fold ($p < 0.05$) and 1.92-fold ($p <$

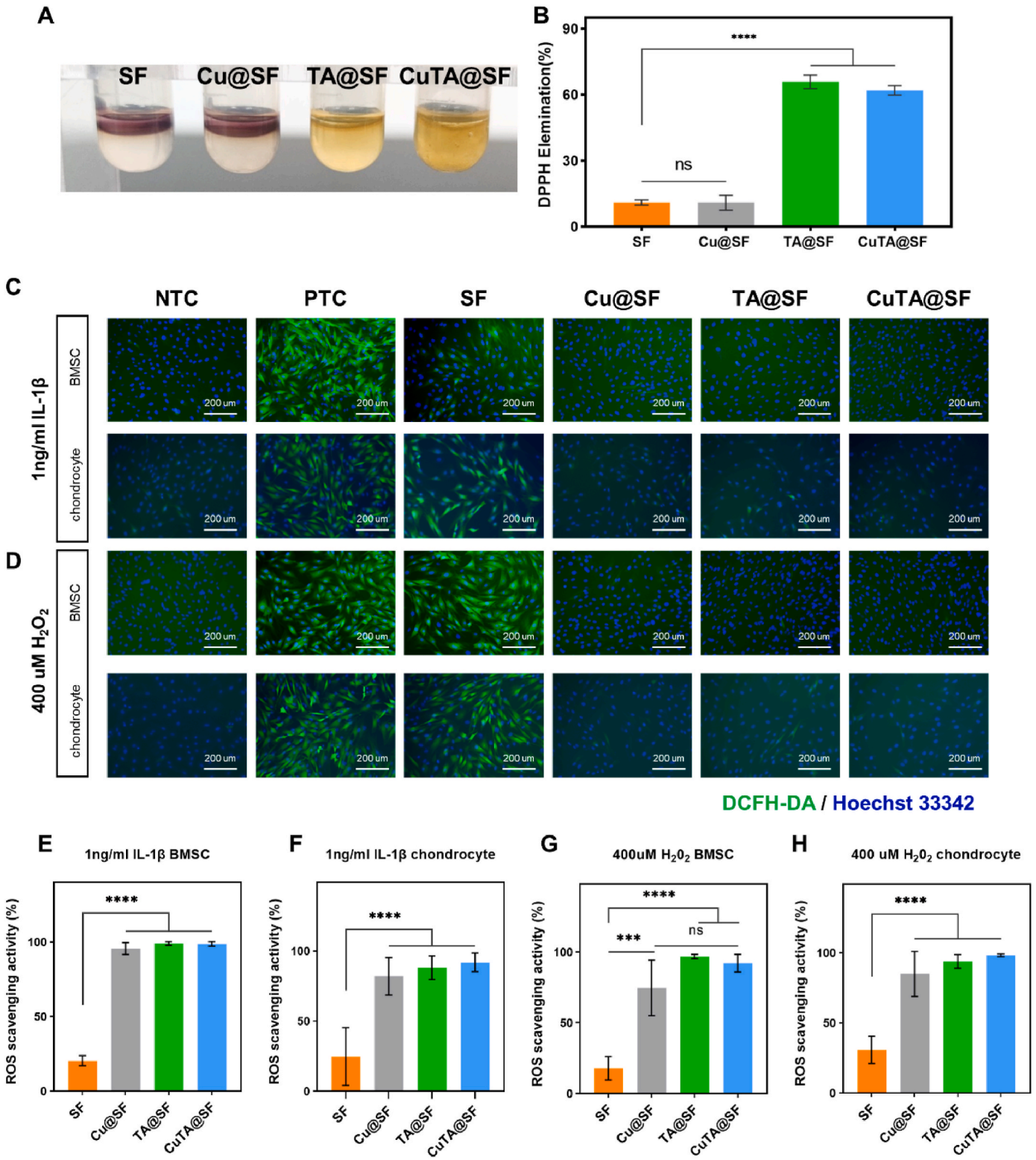

Fig. 4. (A) SF, Cu@SF, TA@SF and CuTA@SF hydrogels in DPPH working solution. (B) DPPH elimination rate of SF, Cu@SF, TA@SF and CuTA@SF hydrogels. (C) Fluorescence images of intracellular ROS level of DCFH-DA treated BMSCs and chondrocytes cultured in growth medium with or without 1 ng/ml IL-1β and the extract of hydrogels. The product of the reaction between ROS and the DCFH-DA showed green fluorescence. Hoechst 33342 was used to stain the nuclei (blue). (D) Fluorescence images of intracellular ROS level of DCFH-DA treated BMSCs and chondrocytes cultured in growth medium with or without 400 μM H_2O_2 and the extract of hydrogels. (E–H) ROS scavenging activity of SF, Cu@SF, TA@SF and CuTA@SF. Results were shown as mean ± SD. ***$p < 0.001$, ****$p < 0.0001$.

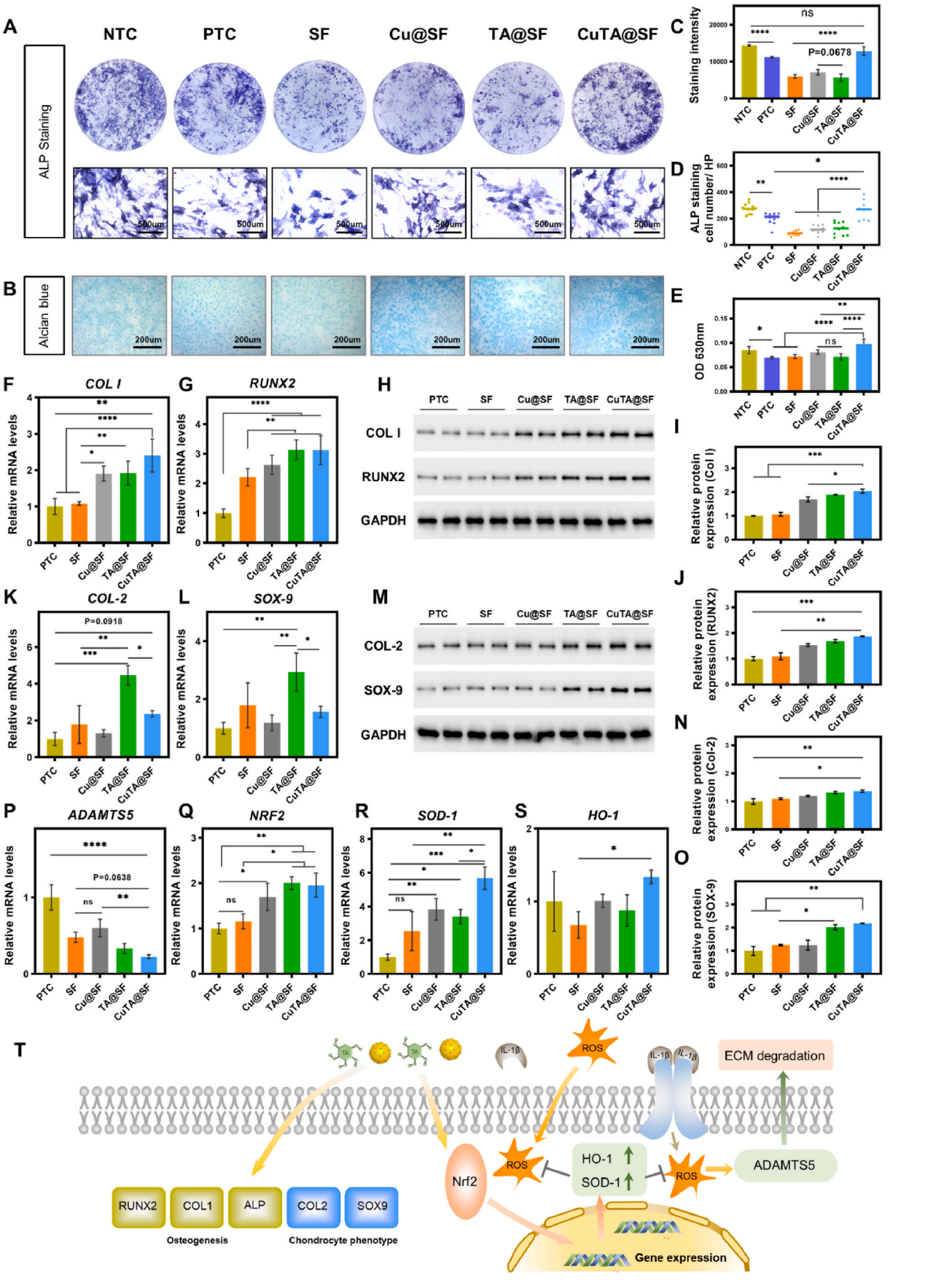

(caption on next page)

Fig. 5. (A) Stereoscope and microscopic images of BMSCs stimulated with 1 ng/ml IL-1β co-stained with ALP and DAPI. (B) Images of chondrocytes stimulated with 1 ng/ml IL-1β stained with Alcian blue. (C) Quantification of ALP staining. (D) The number of ALP positive-stained cells. (E) Quantification of Alcian blue staining. Gene expression levels of osteogenic associated genes *COL I* (F) and *RUNX2* (G) were measured at day 7. The grayscale maps of western blots for BMSC (H) and the corresponding quantification for Col I (I), RUNX2 (J) at day 7. Gene expression level of chondrocyte phenotype associated genes *COL-2* (K) and *SOX-9* (L) was measured with qPCR at day 5. The grayscale maps of western blots for chondrocyte (M) and the corresponding quantification for Col-2 (N), SOX-9 (O) at day 5. Gene expression level of ECM degradation-related enzyme *ADAMTS5* (P) was measured with qPCR. Gene expression levels of Nrf2 pathway-related genes *NRF2* (Q), *SOD-1* (R) and *HO-1* (S) were measured with qPCR at day 5. (T) The proposed model for the protective effect of CuTA@SF in OCD, wherein it inhibited ECM degradation induced by IL-1β via the Nrf2/SOD-1, HO-1 pathway. The effects of CuTA@SF on BMSCs osteogenesis and chondrocyte phenotype maintaining. Results were shown as mean ± SD. *$p < 0.05$, **$p < 0.01$, ***$p < 0.001$, ****$p < 0.0001$.

0.05) compared with PTC, respectively (Fig. 5F). The expression of *RUNX2* for CuTA@SF, TA@SF and Cu@SF was significantly higher than that of SF (Fig. 5G). Osteogenic differentiation markers (Col-1, RUNX2) were also evaluated with WB analysis. Consistent with the PCR result, the expression level of Col I and Runx2 were elevated with the treatment of CuTA@SF at day 7 (Fig. 5H–J). Taken together, CuTA@SF hydrogel showed excellent pro-osteogenic potential under the inflammatory environment as evidenced by both ALP staining and osteogenic gene expression.

To explore whether CuTA@SF could maintain chondrocyte phenotype under the inflammatory environment, primary chondrocytes were cultivated with the growth medium containing the extract of hydrogels with the stimulation of 1 ng/ml IL-1β to evaluate the protective effect for chondrocyte ECM. Alcian blue staining was used to compare the deposition of ECM for different groups after 5 days of induction. The staining images and further quantitative analysis showed poorer staining of PTC with the stimulation of 1 ng/ml IL-1β compared with NTC (Fig. 5B, E), consistent with previous studies that inflammatory factors promoted the degradation of ECM [11,13,92]. CuTA@SF exhibited the strongest staining in contrast to SF, Cu@SF and TA@SF (Fig. 5B), which was further verified by quantitative analysis at 630 nm wavelength (Fig. 5E).

The expression levels of chondrocyte markers, ECM degradation enzyme and Nrf2 pathway-related genes were evaluated with q-PCR. The results showed that the expression of *ADAMTS5*, a pivotal ECM-degrading enzyme of cartilage, for CuTA@SF was downregulated compared with that of PTC ($p < 0.0001$), SF ($p = 0.0638$) and Cu@SF ($p < 0.01$) (Figure 5P). And there was no significant difference between the group of SF, Cu@SF and TA@SF. The gene expression of *COL-2* and *SOX-9* of CuTA@SF was 2.365-fold and 1.562-fold respectively compared with that of PTC, although no significant difference was observed. TA@SF showed the highest gene expression of *COL-2* (4.45-fold for TA@SF vs PTC, $p < 0.001$) and *SOX-9* (2.93-fold for TA@SF vs PTC, $p < 0.01$) (Fig. 5K and L), indicating TA as a biomolecule possesses the potential to maintain chondrocyte phenotype. Despite its excellent potential for cartilage phenotype maintenance, the matrix deposition performance of TA@SF manifested in GAG was inferior to that of CuTA@SF. We further explored the chondrogenic proteins (Col-2, SOX-9) expression affected by hydrogels with WB analysis. The expression of Col-2, SOX-9 was significantly upregulated in CuTA@SF compared with PTC and SF at day 5 (Fig. 5M − O), confirming the chondroprotective effect of CuTA@SF following the IL-1β-induced inflammatory environment. These results collectively indicated that CuTA@SF could rescue the degradation of ECM under inflammatory environment and the potential mechanism would be discussed in the following experiment. Nrf2, a member of the capncollar-basic leucine zipper (CNC-bZIP) transcription activator family, exists in the cytoplasm in an inactive state under physiological conditions. Under the oxidative stress and inflammation environment, the configuration of Nrf2 changes and Nrf2 will transfer to the nucleus to combine with antioxidant response elements (ARE) to regulate the expression of antioxidant enzymes SOD-1 and HO-1. Previous works have shown that the Nrf2 pathway protected the cartilage ECM from degradation caused by inflammatory factors and oxidative stress [13]. We performed qPCR to evaluate the mRNA expression level of *NRF2*, *SOD-1* and *HO-1*. The data revealed that the expression levels of *NRF2*, *SOD-1* and *HO-1* were elevated with the incorporation of CuTA nanozyme. Cu@SF (1.69-fold, $p < 0.05$ for Cu@SF vs PTC), TA@SF (2.00-fold, $p < 0.01$ for TA@SF vs PTC) and CuTA@SF (1.95-fold, $p < 0.01$ for CuTA@SF vs PTC) presented a higher mRNA level of *NRF2* (Figure 5Q), indicating the activation of this pathway. Expression levels of the downstream gene (*SOD-1*, *HO-1*) exhibited the same trend (Figure 5R, S) in the CuTA@SF group, which was consistent with the detection of intracellular ROS levels (Fig. 4C and D).

ROS was also considered to be associated with the cell death of post-traumatic injury [93]. The excellent antioxidant capacity of CuTA@SF may protect the cell from ROS-induced cell death, thereby promoting cell proliferation, which was corresponding to the CCK8 result showing CuTA@SF had the highest proliferation rate compared with other groups. We further evaluated the proliferation of BMSCs and chondrocytes in a simulated injury microenvironment (1 ng/ml IL-1 and 400 μm H_2O_2) for 3 days. Under the stimulation of IL-1β, CuTA@SF displayed an increased proliferation rate compared with SF in BMSCs and chondrocytes (Figs. S7A and B), suggesting its superior ability to modulate inflammatory environments. In addition, H_2O_2 was employed to generate oxidative stress in cells. As previously noted, TA could reverse H_2O_2-induced cell damage [94]. TA@SF and CuTA@SF had a greater proliferation rate than SF, according to the CCK8 results of BMSCs (Fig. S7C). After 3 days of culturing, TA@SF and CuTA@SF also demonstrated increased proliferation compared to SF in chondrocytes, although there was no significant difference between the four groups (Fig. S7D).

Taken together, ROS was generated under IL-1β induction, leading to ECM degeneration. CuTA nanozymes improved the antioxidant capacity through Nrf2 pathway to modulate oxidative stress. Furthermore, CuTA nanozymes promoted osteogenic gene expression (*COL I* and *RUNX2*) and maintain the chondrocyte phenotype under inflammatory microenvironments (Figure 5T). Overall, CuTA@SF hydrogel was able to modify the local microenvironment in the presence of inflammatory factors, thereby holding promises for OCD regeneration.

3.6. The proteomics analysis of CuTA@SF hydrogel on BMSCs and chondrocytes

Proteomics analysis was conducted to detect the underlying mechanism of cellular behavior influenced by CuTA@SF hydrogel. We compared the influence of SF and CuTA@SF hydrogels on BMSCs and chondrocytes in the presence of IL-1β. Heatmap showed differential protein expression (Fig. 6A and B). The samples of CuTA@SF possessed different protein expressions compared with SF in principal component analysis (Fig. 6D, F). In the group of BMSCs, 2134 proteins were identified. In Fig. 6C, the volcano map showed 97 differentially expressed proteins including 48 up-regulated and 49 down-regulated proteins, marked in red and blue respectively. In the group of chondrocytes, there were 2762 identified proteins and 146 differentially expressed proteins including 74 up-regulated and 72 down-regulated proteins (Fig. 6E).

We performed GO enrichment analysis to further evaluate the pathways affected by CuTA@SF. In BMSCs, the up-regulated proteins were enriched in “tissue migration”, “chemical homeostasis”, “smooth muscle cell migration”, “regulation of vasculature development” and “muscle contraction”, which were closely related to the process of osteogenesis. In vitro experiments showed that the CuTA@SF could eliminate intracellular ROS and counteracted the inflammatory

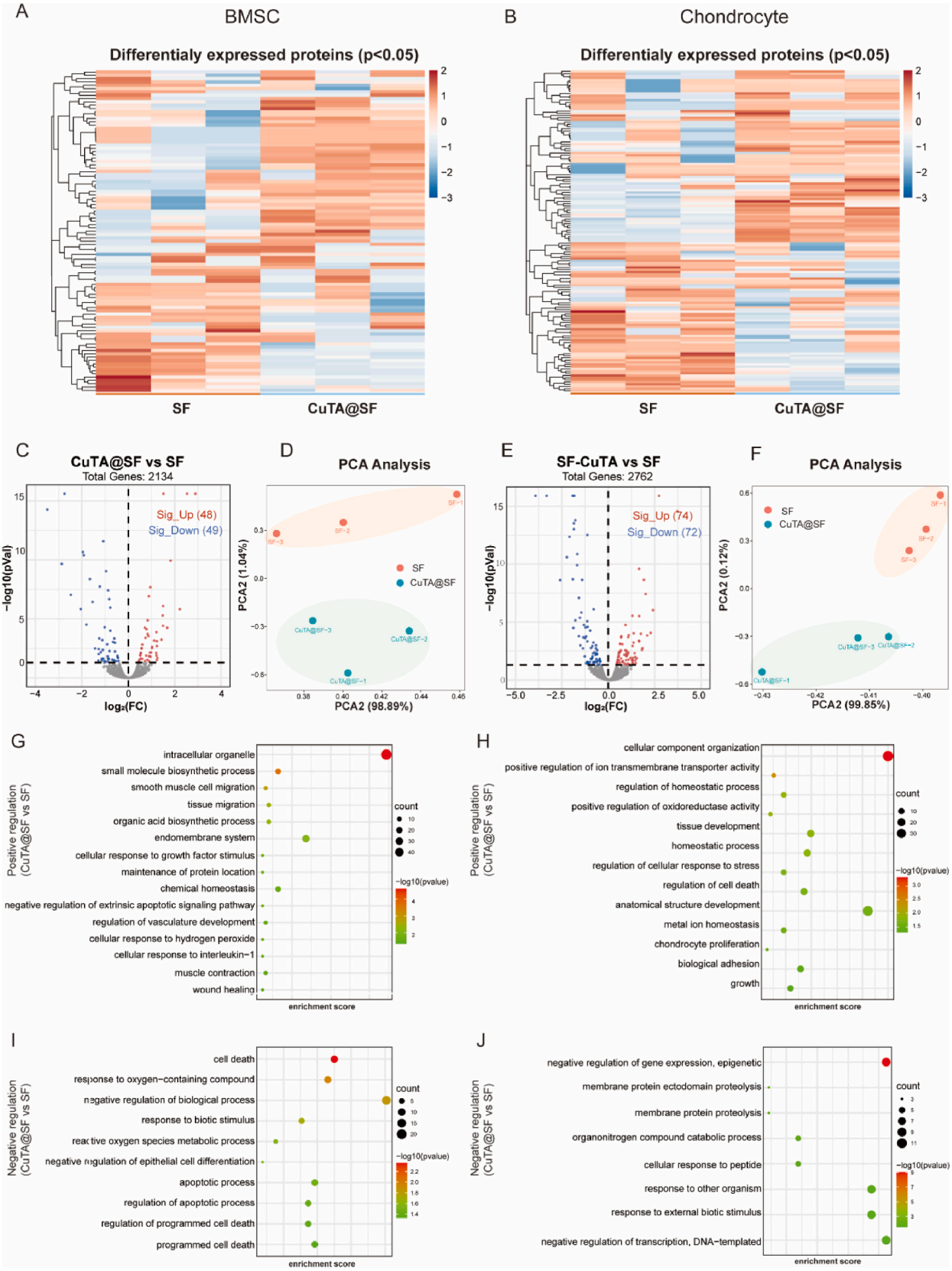

Fig. 6. Heatmap of differentially expressed proteins between CuTA@SF and SF in BMSC (A) and chondrocyte (B). (C) Volcano plot shows protein expression levels (CuTA@SF vs SF) including up-regulated and down-regulated proteins in BMSCs. (D) PCA plot of CuTA@SF and SF (n = 3) in BMSCs. (E) Volcano plot shows protein expression levels (CuTA@SF vs SF) including up-regulated and down-regulated proteins in chondrocytes. (F) PCA plot of CuTA@SF and SF (n = 3) in chondrocytes. GO enrichment analysis of up-regulated and down-regulated terms between CuTA@SF and SF for BMSCs (G, I) and chondrocytes (H, J).

microenvironment under the stimulation of IL-1β (Fig. 4C–H, Fig. 5A–S). Some items related to inflammation and antioxidant were also enriched such as "cellular response to interleukin-1", "cellular response to hydrogen peroxide" and "negative regulation of extrinsic apoptotic signaling pathway" (Fig. 6G). The down-regulated proteins were enriched in "cell death" and "apoptotic process", which corresponded to the previous CCK-8 and Live/dead staining (Fig. 3A–F) that CuTA@SF promoted proliferation and maintained cell viability (Fig. 6I). In chondrocytes, the most up-regulated proteins were enriched in "tissue development", "metal ion homeostasis" and "chondrocyte proliferation" (Fig. 6H). The down-regulated proteins were enriched in "membrane protein proteolysis" and "response to other organisms", indicating that CuTA@SF had the potential to promote cartilage regeneration after injury via maintaining microenvironmental homeostasis (Fig. 6J). The molecular function part of GO enrichment analysis was further displayed in enrichment chord analysis. In BMSCs, up-regulated proteins were enriched in "oxidoreductase activity", "metal ion binding" and "catalytic activity". Pathway-related proteins were displayed in Fig. S8A. The enrichment chord analysis of chondrocytes demonstrated that up-regulated proteins were involved in the "enzyme activator activity", "enzyme regulator activity", "nitric-oxide synthase binding" and "cytoskeletal protein binding" (Fig. S8B).

Differentially expressed proteins were employed to map protein-protein interaction (PPI) networks. In the group of BMSCs, the result verified that EGR1, TAGLN, CSRP1 were up-regulated proteins exerting important functions (Fig. S9A). EGR1 is a transcription factor regulating cell differentiation and growth. And previous research confirmed that EGR1 substantially contributed to the osteogenesis of stem cells and tissue repairment after injury [95,96]. TAGLN acts as an actin-crosslinking/gelling protein that regulates the cytoskeleton for cell proliferation, migration and differentiation to adapt to external stimuli [97]. CSRP1 is a cysteine-rich protein that effectively promotes the growth and development of the skeletal system [98–100]. In the group of chondrocytes, FN1, Uqcrfs1, Ndufb10, ATP5D, Cox17 were hub up-regulated proteins in the PPI network (Fig. S9B). FN1(fibronectin1) is a biomolecule located in the ECM involving cell migration and adhesion via cell-ECM interaction [101]. The up-regulation of Uqcrfs1, Ndufb10 and ATP5D may have contributed to the increase in electron transfer and energy production in the mitochondrial respiratory chain. Cox17 was thought to transport intracellular copper ions and protect the cell from oxidative stress [102].

We also conducted gene set enrichment analysis (GSEA) to detect subtle protein expression changes. In the group of BMSCs, the results of GSEA showed that CuTA@SF up-regulated ECM related pathways under osteogenic induction such as "type I collagen synthesis in the context of osteogenesis imperfecta", "collagen formation", "ECM organization", "ECM regulators", "collagen biosynthesis and modifying enzymes" and "ECM proteoglycans" (Fig. S9C). Consistent with the PCR results under osteogenic induction (Fig. 5G), GSEA also exhibited enhanced RUNX2 expression and activity (Fig. S9C), which is crucial for osteoblast differentiation and bone morphogenesis. TGFβ1 and WNT signaling pathways, which are traditional osteogenesis-related pathways, were found to be up-regulated under the incubation of CuTA@SF in GSEA analysis (Fig. S9C). HO-1 (HMOX-1), a downstream regulatory gene of the Nrf2 pathway, plays the role of antioxidant and protecting cells from oxidative stress. HO-1 related pathways like "regulation of HMOX-1 expression and activity" and "cytoprotection by HMOX-1" exhibited an upward trend (Fig. S9C). Consistent with GO analysis, the term "apoptotic execution phase" was down-regulated in GSEA (Fig. S9C). In the group of chondrocytes, the GSEA analysis of "interleukin-1 signaling" and "interleukin-1 family signaling" (Fig. S9D) indicated that CuTA@SF could reduce the unfavorable effect of IL-1β, which confirmed the potential mechanism that CuTA@SF could protect the ECM of cartilage under the inflammatory factor stimulation. There were up-regulated pathways such as "G2 M cell cycle", "cell cycle genes in IR response 24hr", "apoptosis modulation and signaling" and "EGR 2 targets up" (Fig. S9D), which implied that the CuTA@SF hydrogel could accelerate cell proliferation compared with SF.

Collectively, the proteomic analysis has confirmed that CuTA@SF hydrogel elevated the expression of the proteins of osteogenesis-related pathways and influenced apoptosis signaling pathways to facilitate cell proliferation. Moreover, the antioxidant properties were also enhanced and the inflammatory factor signal was down-regulated with the treatment of CuTA@SF hydrogel, thus CuTA@SF hydrogel is excellent in modulating the undesired microenvironment and improving OCD regeneration.

3.7. In vivo evaluation of CuTA@SF hydrogel for OCD repair

Hydrogels were implanted into the rabbit OCD and samples were collected at 12 weeks post-implantation to evaluate the efficiency of OCD regeneration. The gross observation revealed that the SF-based hydrogels were biocompatible since there was no purulent exudation or inflammatory response in the joints of each sample. The defect areas of each group were filled with white neo-tissue and cracks existed in the regeneration area of CTL, SF, Cu@SF and TA@SF groups. However, the repaired tissue in CuTA@SF had a regular surface and was well integrated with surrounding tissues (Fig. 7A). Cross-sectional views showed that TA@SF and CuTA@SF hydrogels were almost completely degraded (Fig. 7B). Previous studies have reported that the degradation rate of silk hydrogel in vivo was associated with the enzymatic hydrolysis and hydrophilic reaction in the implant area as well as the microstructure of hydrogels [103]. The incorporation of TA enhanced the hydrophilicity of the SF-based material, thus may accelerate the hydrolysis and enzymatic hydrolysis process and facilitate the proper degradation of CuTA@SF and TA@SF hydrogels in vivo. In contrast, most of SF and Cu@SF hydrogels still existed in the defect area, hindering the growth of new tissue, which would be further displayed in histological staining and CT images.

In the micro-CT images (Fig. S10), it was found that a large void remained in the center of the defect region in CTL, indicating that the spontaneous regeneration of BMSC is insufficient in the repair of critical-size defects. In marked contrast, there were calcified tissues filled and formed a bony connection with surrounding subchondral bone in Cu@SF, TA@SF and CuTA@SF (Fig. S10). Three-dimensional reconstruction also exhibited that the area of regenerated trabecular bone was the largest in CuTA@SF (Fig. 7C). To further evaluate the efficiency of subchondral bone regeneration in different groups, we performed a quantitative micro-CT analysis. The BMD of CuTA@SF reached 0.24 ± 0.05 g/cm^3, which was higher than that of CTL (0.13 ± 0.02 g/cm^3, $p < 0.01$ for CuTA@SF vs CTL), SF (0.13 ± 0.03 g/cm^3, $p < 0.01$ for CuTA@SF vs SF), Cu@SF (0.18 ± 0.03 g/cm^3, $p = 0.0785$ for CuTA@SF vs Cu@SF) and TA@SF (0.17 ± 0.02 g/cm^3, $p = 0.0874$ for CuTA@SF vs TA@SF) (Fig. 7D). Although the improvement was not significant, the BMD of Cu@SF and TA@SF was higher than CTL, implying the implantation of hydrogels facilitated the growth of subchondral bone. The unfunctionalized SF hydrogel had a weak ability to promote the regeneration of subchondral bone which showed the value of BMD similar to that of CTL. The results of BV/TV and TB.N showed a unanimous trend between groups as BMD (Fig. 7E and F). CuTA@SF possessed the highest values of BV/TV and TB.N compared with other groups. TA@SF and Cu@SF performed better than CTL and SF in the regeneration of subchondral bone as evaluated by the above analysis. The subchondral bone regeneration effect of CuTA@SF was the best, which was consistent with the in vitro results of ALP staining (Fig. S3J). There was no apparent difference in TB.Th between groups (Fig. 7G), which indicated that the thickness of the regenerated trabecular bone was similar. Hence, the results of BMD, BV/TV and TB.N demonstrated that CuTA@SF improved the quality of trabecular bone regeneration compared with other hydrogels.

Subsequently, the sections of the femoral condyle sample were stained with HE (Fig. S11). In HE staining, all samples had no occurrence

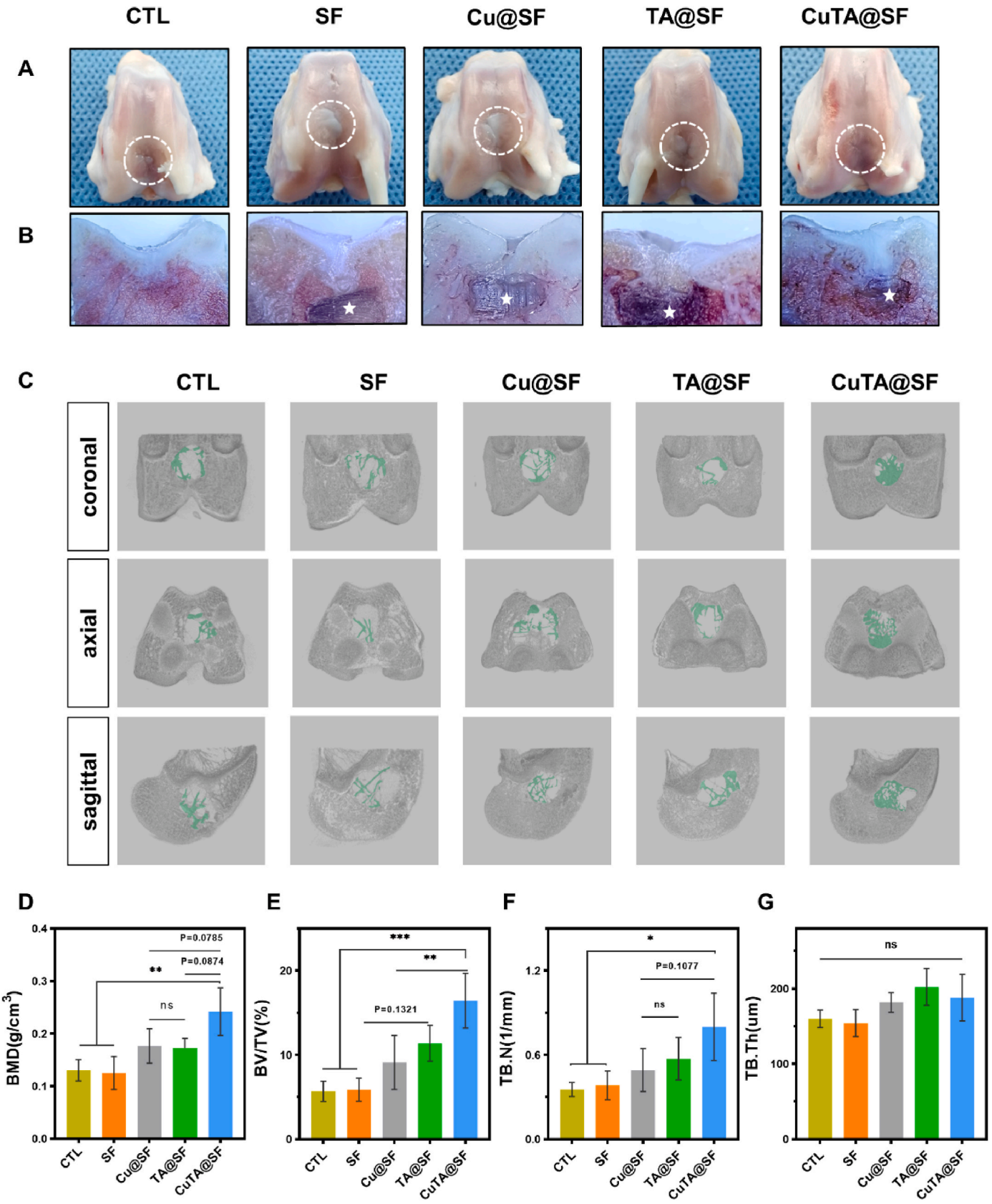

Fig. 7. General view (A) and cross-sectional view (B) of the femoral condyles of rabbit osteochondral defect model in CTL, SF, Cu@SF, TA@SF and CuTA@SF at 12 weeks after surgery. The residue hydrogels were marked by an asterisk. (C) Three-dimensional reconstruction images of three planes (coronal, axial, sagittal) using the micro-CT data of CTL, SF, Cu@SF, TA@SF and CuTA@SF. The green color stands for newly formed subchondral bone. Bone mass analysis of the obtained samples with quantitative micro-CT for (D) bone mineral density (BMD), (E) bone volume/total volume (BV/TV), (F) trabecular numbers (Tb. N) and (G) trabecular thickness (Tb. Th). Results were shown as mean ± SD, *$p < 0.05$, **$p < 0.01$, ***$p < 0.001$.

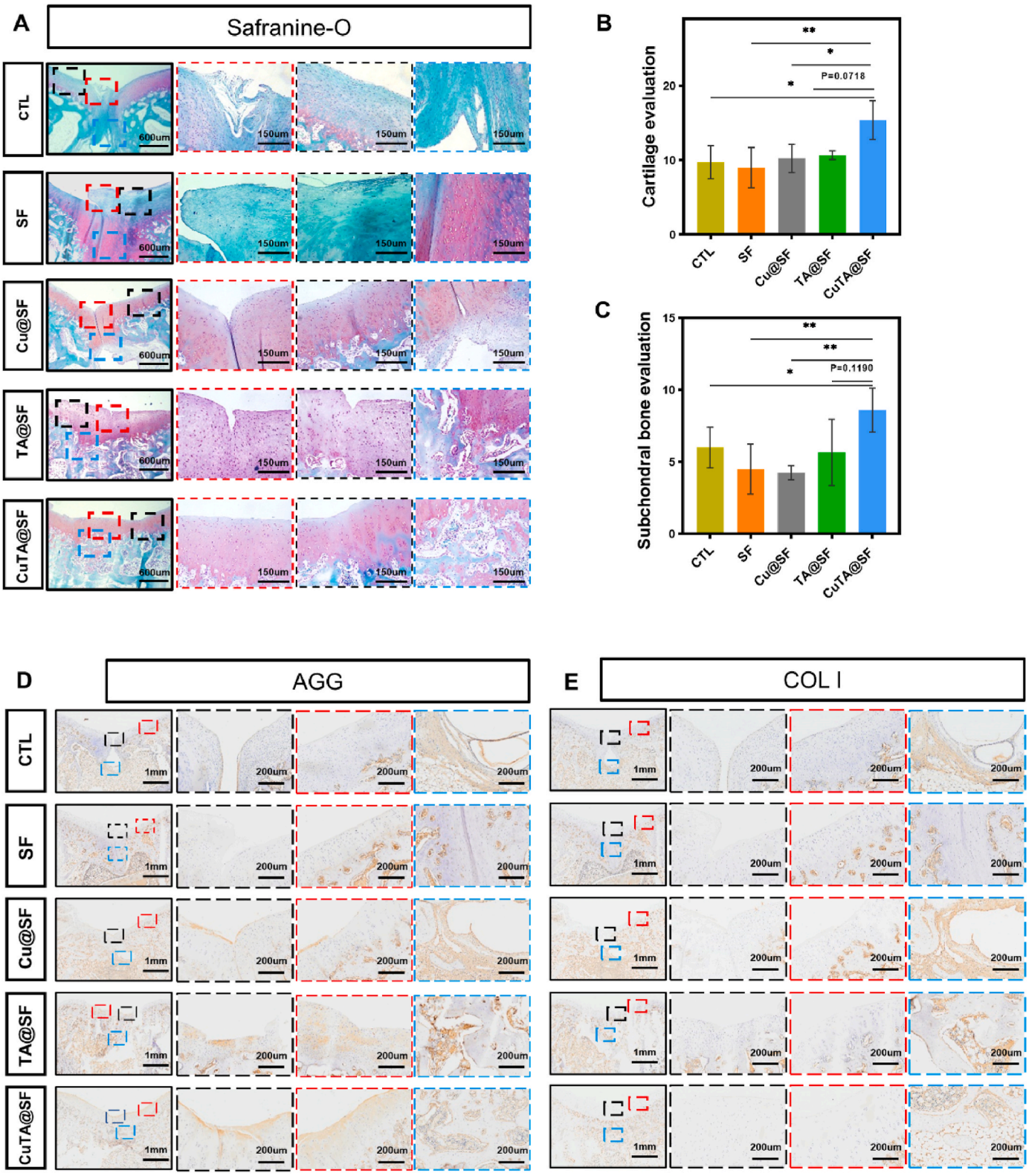

Fig. 8. (A) S/O staining image of regenerated osteochondral samples at 12 weeks after surgery. The evaluation of cartilage (B) and subchondral bone (C) regeneration using the established histological scoring system. Immunohistochemical staining of regenerated osteochondral tissue for AGG (D) and Col I (E) at 12 weeks after surgery. Results were shown as mean ± SD, *p < 0.05, **p < 0.01.

of osteoarthritis. Although the defect region of each group had more than 50% neo-tissue filling, the physical stratified structure of cartilage and subchondral bone was varied. The clear boundary between cartilage and the subchondral bone area was lost in CTL, SF and Cu@SF, especially in the middle of the defect. In contrast, the cartilage and subchondral bone structure of TA@SF and CuTA@SF were clear, and the tide line was visible (Fig. S11). The samples were further stained with S/O (Fig. 8A) to evaluate the distribution of GAG in newly formed tissue. Previous studies demonstrated that uncontrolled self-repair via endogenous stem cells often leads to the production of fibrocartilage [67]. In S/O staining, the regenerated disorganized fibrous tissue filled the cartilage layer and subchondral bone layer in CTL, demonstrating limited and inefficient autonomous regeneration. In SF, the subchondral bone region of the defect was filled with positive safranin O-stained tissue and the cartilage region of the defect was covered with fast green-stained fibrous tissue, which revealed immature and incomplete regeneration by pure SF hydrogel. Efficient repair of subchondral bone provides sufficient blood supply and structural support for articular cartilage. In line with previous in vitro studies, the extract of SF and Cu@SF have insufficient ability to stimulate osteogenic differentiation (Fig. 3J). There were only fiber tissue and few trabecular bones formed in the subchondral bone area of SF and Cu@SF. In TA@SF, the boundary between cartilage and subchondral bone was distinct. But the characteristic of hyaline chondrocytes was not obvious in the newly formed cartilage of TA@SF. Notably, CuTA@SF exhibited excellent repair performance, showing the formation of neo-cartilage tissue with a typical round shape of articular chondrocyte. Newly formed cartilage tightly integrated with the adjacent host cartilage in CuTA@SF. The subchondral region of the defect was filled with newly formed subchondral bone and had scattered positive safranin O-stained tissues, indicating the orderly tissue repair in the endochondral ossification process supported by CuTA@SF hydrogel (Fig. 8A). The histological score based on S/O staining was carried out to assess the regeneration of cartilage. CuTA@SF had the highest score (15.40 $\pm$ 2.61) compared with CTL (9.75 $\pm$ 2.22, $P < 0.05$ for CuTA@SF vs CTL), SF (9.00 $\pm$ 2.71, $P < 0.01$ for CuTA@SF vs SF), Cu@SF (10.25 $\pm$ 1.89, $P < 0.05$ for CuTA@SF vs Cu@SF) and TA@SF (10.67 $\pm$ 0.58, $P = 0.0718$ for CuTA@SF vs TA@SF) (Fig. 8B). The following histological score of subchondral bone demonstrated that CuTA@SF hydrogel had the highest ability to promote subchondral bone formation, as evidenced by the values of CuTA@SF (8.60 $\pm$ 1.52), TA@SF (5.67 $\pm$ 2.31), Cu@SF (4.25 $\pm$ 0.50), SF (4.50 $\pm$ 1.73) and CTL (6.00 $\pm$ 1.41) (Fig. 8C).

The regenerated tissue in the cartilage region showed considerable positive toluidine blue staining in all samples. But the top layer of CTL and SF displayed relatively poor toluidine blue staining indicating the formation of fibrous cartilage (Fig. S12). Consistent with S/O staining, CuTA@SF showed more hyaline cartilage and strong toluidine blue staining similar to normal cartilage. Furthermore, immunohistochemistry staining of COL I and AGG were performed to characterize the ECM-specific proteins in the newly formed osteochondral tissue. The most intense positive AGG staining was detected in the cartilage layer of CuTA@SF, confirming the effective formation of hyaline cartilage. Relatively weak positive AGG staining was found in Cu@SF and TA@SF. There was almost no positive AGG staining area in the cartilage layer of CTL and SF (Fig. 8D). The positive staining of COL I was observed in the subchondral regions of all samples. CuTA@SF had the largest orderly positive staining area of COL I in the regenerated subchondral bone region, suggesting effective trabecular bone regeneration (Fig. 8E). Taken together, the above results demonstrated that the CuTA@SF hydrogel provided a suitable microenvironment for enhanced OCD regeneration in vivo.

4. Conclusion

In this study, we fabricated a novel multifunctional CuTA@SF hydrogel with synergistic effects of anti-oxidant, anti-inflammation and antibacterial properties to improve OCD regeneration. The CuTA nanozyme established before was used for scavenging ROS in cigarette smoke or as antibacterial material, but has not been explored for regenerative applications. To our knowledge, it is the first study that the combination of CuTA nanozyme and silk fibroin was employed in the regeneration of osteochondral defects. CuTA@SF possessed the capacity of scavenging active free radicals like DPPH and moderating the elevated level of intracellular ROS, thus maintaining the homeostasis between oxidation and antioxidant. CuTA@SF was founded to enhance the proliferation of BMSCs and chondrocytes, as well as inhibit the growth of *Staphylococcus aureus*, the most common pathogen in orthopedics. Under inflammatory microenvironment, CuTA@SF promoted the osteogenic differentiation of BMSCs and enhanced the deposition of cartilage-specific ECM, showing the ability to modulate the local inflammatory environment. In vivo rabbit OCD model confirmed the excellent biocompatibility and efficient OCD regeneration ability of CuTA@SF. In summary, the novel multifunctional CuTA@SF hydrogel developed in this study provides a potential scaffold for clinical treatment of OCD.

Ethics approval and consent to participate

The ethical inspection committee of the Nanjing first hospital approved the study protocol (Ethical Approval Number: KY20190918-01).

CRediT authorship contribution statement

Zhicheng Cao: Conceptualization, Methodology, Data curation, Formal analysis, Funding acquisition, Project administration, Writing – original draft. **Hongmei Wang:** Data curation, Formal analysis, Investigation. **Jialin Chen:** Methodology, Project administration, Funding acquisition, Resources. **Yanan Zhang:** Data curation, Formal analysis, Investigation. **Qingyun Mo:** Data curation, Formal analysis, Investigation. **Po Zhang:** Data curation, Formal analysis. **Mingyue Wang:** Data curation, Formal analysis, Investigation. **Haoyang Liu:** Data curation, Writing – review & editing. **Xueyang Bao:** Data curation, Formal analysis. **Yuzhi Sun:** Data curation, Formal analysis. **Wei Zhang:** Conceptualization, Methodology, Writing – review & editing, Project administration, Funding acquisition, Resources. **Qingqiang Yao:** Conceptualization, Methodology, Project administration, Funding acquisition, Resources.

Declaration of competing interest

The authors declared that they have no conflicts of interest to this work. We declare that we do not have any commercial or associative interest that represents a conflict of interest in connection with the work submitted.

Acknowledgments

This work was financially supported by the National Natural Science Foundation of China (81901903, 5171101275, 81771985, 81972042, 82072400), the Natural Science Foundation of Jiangsu Province (BK20190356, BK20190354, BK20200001, BE2019736, BE2019679), the Zhishan Scholars Programs of Southeast University and the Postgraduate Research and Innovation Project of Jiangsu Province (SJCX 21_0637).

Appendix A. Supplementary data

Supplementary data to this article can be found online at https://doi.org/10.1016/j.bioactmat.2022.05.025.

References

[1] Y. Jiang, R.S. Tuan, Origin and function of cartilage stem/progenitor cells in osteoarthritis, Nat. Rev. Rheumatol. 11 (4) (2015) 206–212.
[2] B.M. Saltzman, J.C. Riboh, Subchondral bone and the osteochondral unit: basic science and clinical implications in sports medicine, Sport Health 10 (5) (2018) 412–418.
[3] H. Kwon, W.E. Brown, C.A. Lee, D. Wang, N. Paschos, J.C. Hu, K.A. Athanasiou, Surgical and tissue engineering strategies for articular cartilage and meniscus repair, Nat. Rev. Rheumatol. 15 (9) (2019) 550–570.
[4] Z. Wang, H. Le, Y. Wang, H. Liu, Z. Li, X. Yang, C. Wang, J. Ding, X. Chen, Instructive cartilage regeneration modalities with advanced therapeutic implantations under abnormal conditions, Bioact. Mater. 11 (1800) 317–338.
[5] A.R. Armiento, M.J. Stoddart, M. Alini, D. Eglin, Biomaterials for articular cartilage tissue engineering: learning from biology, Acta Biomater. 65 (2018) 1–20.
[6] Z.W. Wang, L. Chen, X.R. Hao, Z.A. Qu, S.B. Huang, X.J. Ma, J.C. Wang, W. M. Wang, Elevated levels of interleukin-1beta, interleukin-6, tumor necrosis factor-alpha and vascular endothelial growth factor in patients with knee articular cartilage injury, World J Clin Cases 7 (11) (2019) 1262–1269.
[7] J. Riegger, H. Joos, H.G. Palm, B. Friemert, H. Reichel, A. Ignatius, R.E. Brenner, Antioxidative therapy in an ex vivo human cartilage trauma-model: attenuation of trauma-induced cell loss and ECM-destructive enzymes by N-acetyl cysteine, Osteoarthritis Cartilage 24 (12) (2016) 2171–2180.
[8] H. Katagiri, L.F. Mendes, F.P. Luyten, Definition of a critical size osteochondral knee defect and its negative effect on the surrounding articular cartilage in the rat, Osteoarthritis Cartilage 25 (9) (2017) 1531–1540.
[9] Z.W. Wang, L. Chen, X.R. Hao, Z.A. Qu, S.B. Huang, X.J. Ma, J.C. Wang, W. M. Wang, Elevated levels of interleukin-1 beta, interleukin-6, tumor necrosis factor-alpha and vascular endothelial growth factor in patients with knee articular cartilage injury, World. J. Clin. Cases. 7 (11) (2019) 1262–1269.
[10] C.T. Jayasuriya, Y. Chen, W. Liu, Q. Chen, The influence of tissue microenvironment on stem cell-based cartilage repair, Ann. N. Y. Acad. Sci. 1383 (1) (2016) 21–33.
[11] X. Liu, Y. Xu, S. Chen, Z. Tan, K. Xiong, Y. Li, Y. Ye, Z.P. Luo, F. He, Y. Gong, Rescue of proinflammatory cytokine-inhibited chondrogenesis by the antiarthritic effect of melatonin in synovium mesenchymal stem cells via suppression of reactive oxygen species and matrix metalloproteinases, Free Radic. Biol. Med. 68 (2014) 234–246.
[12] D.C. Lacey, P.J. Simmons, S.E. Graves, J.A. Hamilton, Proinflammatory cytokines inhibit osteogenic differentiation from stem cells: implications for bone repair during inflammation, Osteoarthritis Cartilage 17 (6) (2009) 735–742.
[13] S. Zuo, W. Zou, R.M. Wu, J. Yang, J.N. Fan, X.K. Zhao, H.Y. Li, Icariin alleviates IL-1beta-induced matrix degradation by activating the Nrf2/ARE pathway in human chondrocytes, Drug Des. Dev. Ther. 13 (2019) 3949–3961.
[14] Y. Li, M. Chen, J. Yan, W. Zhou, S. Gao, S. Liu, Q. Li, Y. Zheng, Y. Cheng, Q. Guo, Tannic acid/Sr(2+)-coated silk/graphene oxide-based meniscus scaffold with anti-inflammatory and anti-ROS functions for cartilage protection and delaying osteoarthritis, Acta Biomater. 126 (2021) 119–131.
[15] F. Atashi, A. Modarressi, M.S. Pepper, The role of reactive oxygen species in mesenchymal stem cell adipogenic and osteogenic differentiation: a review, Stem Cell. Dev. 24 (10) (2015) 1150–1163.
[16] R.A. Denu, P. Hematti, Effects of oxidative stress on mesenchymal stem cell biology, Oxid. Med. Cell. Longev. (2016), 2989076, 2016.
[17] K. Morita, T. Miyamoto, N. Fujita, Y. Kubota, K. Ito, K. Takubo, K. Miyamoto, K. Ninomiya, T. Suzuki, R. Iwasaki, M. Yagi, H. Takaishi, Y. Toyama, T. Suda, Reactive oxygen species induce chondrocyte hypertrophy in endochondral ossification, J. Exp. Med. 204 (7) (2007) 1613–1623.
[18] R. Zuo, Y. Wang, J. Li, J. Wu, W. Wang, B. Li, C. Sun, Z. Wang, C. Shi, Y. Zhou, M. Liu, C. Zhang, Rapamycin induced autophagy inhibits inflammation-mediated endplate degeneration by enhancing nrf2/keap1 signaling of cartilage endplate stem cells, Stem Cell. 37 (6) (2019) 828–840.
[19] D. Cai, S. Yin, J. Yang, Q. Jiang, W. Cao, Histone deacetylase inhibition activates Nrf2 and protects against osteoarthritis, Arthritis Res. Ther. 17 (2015) 269.
[20] L. Zhou, V.O. Gjvm, J. Malda, M.J. Stoddart, Y. Lai, R.G. Richards, K. Ki-Wai Ho, L. Qin, Innovative tissue-engineered strategies for osteochondral defect repair and regeneration: current progress and challenges, Adv Healthc Mater (2020), e2001008.
[21] M. He, X. Gao, Y. Fan, L. Xie, M. Yang, W. Tian, Tannic acid/Mg(2+)-based versatile coating to manipulate the osteoimmunomodulation of implants, J. Mater. Chem. B 9 (4) (2021) 1096–1106.
[22] A. Sivanantham, D. Pattarayan, N. Rajasekar, A. Kannan, L. Loganathan, R. Bethunaickan, S.K. Mahapatra, R. Palanichamy, K. Muthusamy, S. Rajasekaran, Tannic acid prevents macrophage-induced pro-fibrotic response in lung epithelial cells via suppressing TLR4-mediated macrophage polarization, Inflamm. Res. 68 (12) (2019) 1011–1024.
[23] X. He, X. Liu, J. Yang, H. Du, N. Chai, Z. Sha, M. Geng, X. Zhou, C. He, Tannic acid-reinforced methacrylated chitosan/methacrylated silk fibroin hydrogels with multifunctionality for accelerating wound healing, Carbohydr. Polym. 247 (2020) 116689.
[24] J. Zhao, Y. Liu, B. Pan, G. Gao, Y. Liu, S. Liu, N. Liang, D. Zhou, M.G. Vijver, W. Peijnenburg, Tannic acid promotes ion release of copper oxide nanoparticles: impacts from solution pH change and complexation reactions, Water Res. 127 (2017) 59–67.
[25] W. Zhang, C. Ling, H. Liu, A. Zhang, L. Mao, J. Wang, J. Chao, L.J. Backman, Q. Yao, J. Chen, Tannic acid-mediated dual peptide-functionalized scaffolds to direct stem cell behavior and osteochondral regeneration, Chem. Eng. J. 396 (2020).
[26] M.V. Lomova, A.I. Brichkina, M.V. Kiryukhin, E.N. Vasina, A.M. Pavlov, D. A. Gorin, G.B. Sukhorukov, M.N. Antipina, Multilayer capsules of bovine serum albumin and tannic acid for controlled release by enzymatic degradation, ACS Appl. Mater. Interfaces 7 (22) (2015) 11732–11740.
[27] M.I. Din, F. Arshad, Z. Hussain, M. Mukhtar, Green adeptness in the synthesis and stabilization of copper nanoparticles: catalytic, antibacterial, cytotoxicity, and antioxidant activities, Nanoscale Res. Lett. 12 (1) (2017) 638.
[28] J.Y. Lee, H. Lim, J.W. Ahn, D. Jang, S.H. Lee, K. Park, S.E. Kim, Design of a 3D BMP-2-delivering tannylated PCL scaffold and its anti-oxidant, anti-inflammatory, and osteogenic effects in vitro, Int. J. Mol. Sci. 19 (11) (2018).
[29] C.H. Chen, T.Z. Liu, C.H. Chen, C.H. Wong, C.H. Chen, F.J. Lu, S.C. Chen, The efficacy of protective effects of tannic acid, gallic acid, ellagic acid, and propyl gallate against hydrogen peroxide-induced oxidative stress and DNA damages in IMR-90 cells, Mol. Nutr. Food Res. 51 (8) (2007) 962–968.
[30] C. Wang, H. Zhou, H. Niu, X. Ma, Y. Yuan, H. Hong, C. Liu, Tannic acid-loaded mesoporous silica for rapid hemostasis and antibacterial activity, Biomater Sci 6 (12) (2018) 3318–3331.
[31] J.Y. Uriu-Adams, C.L. Keen, Copper, oxidative stress, and human health, Mol. Aspect. Med. 26 (4–5) (2005) 268–298.
[32] T. Liu, B. Xiao, F. Xiang, J. Tan, Z. Chen, X. Zhang, C. Wu, Z. Mao, G. Luo, X. Chen, J. Deng, Ultrasmall copper-based nanoparticles for reactive oxygen species scavenging and alleviation of inflammation related diseases, Nat. Commun. 11 (1) (2020) 2788.
[33] R.H. Yang, G. Li, C.Y. Zhuang, P. Yu, T.J. Ye, Y. Zhang, P.Y. Shang, J.J. Huang, M. Cai, L. Wang, W.G. Cui, L.F. Deng, Gradient bimetallic ion-based hydrogels for tissue microstructure reconstruction of tendon-to-bone insertion, Sci. Adv. 7 (26) (2021).
[34] R. Lin, C. Deng, X. Li, Y. Liu, M. Zhang, C. Qin, Q. Yao, L. Wang, C. Wu, Copper-incorporated bioactive glass-ceramics inducing anti-inflammatory phenotype and regeneration of cartilage/bone interface, Theranostics 9 (21) (2019) 6300–6313.
[35] M. Che, R. Wang, X. Li, H.-Y. Wang, X.F.S. Zheng, Expanding roles of superoxide dismutases in cell regulation and cancer, Drug Discov. Today 21 (1) (2016) 143–149.
[36] T. Fukai, M. Ushio-Fukai, Superoxide dismutases: role in redox signaling, vascular function, and diseases, Antioxidants Redox Signal. 15 (6) (2011) 1583–1606.
[37] L.O. Klotz, C. Sanchez-Ramos, I. Prieto-Arroyo, P. Urbanek, H. Steinbrenner, M. Monsalve, Redox regulation of FoxO transcription factors, Redox Biol. 6 (2015) 51–72.
[38] S. Lin, Y. Cheng, H. Zhang, X. Wang, Y. Zhang, Y. Zhang, L. Miao, X. Zhao, H. Wei, Copper tannic acid coordination nanosheet: a potent nanozyme for scavenging ROS from cigarette smoke, Small 16 (27) (2020), e1902123.
[39] B. Kundu, R. Rajkhowa, S.C. Kundu, X. Wang, Silk fibroin biomaterials for tissue regenerations, Adv. Drug Deliv. Rev. 65 (4) (2013) 457–470.
[40] Z.Y. Chen, Q. Zhang, H.M. Li, Q. Wei, X. Zhao, F.L. Chen, Elastin-like polypeptide modified silk fibroin porous scaffold promotes osteochondral repair, Bioact. Mater. 6 (3) (2021) 589–601.
[41] V.A.M. Gonzaga, A.L. Poli, J.S. Gabriel, D.Y. Tezuka, T.A. Valdes, A. Leitão, C. F. Rodero, T.M. Bauab, M. Chorilli, C.C. Schmitt, Chitosan-laponite nanocomposite scaffolds for wound dressing application, J. Biomed. Mater. Res. B Appl. Biomater. 108 (4) (2020) 1388–1397.
[42] J. Jing, S. Liang, Y. Yan, X. Tian, X. Li, Fabrication of hybrid hydrogels from silk fibroin and tannic acid with enhanced gelation and antibacterial activities, ACS Biomater. Sci. Eng. 5 (9) (2019) 4601–4611.
[43] M. Gosset, F. Berenbaum, S. Thirion, C. Jacques, Primary culture and phenotyping of murine chondrocytes, Nat. Protoc. 3 (8) (2008) 1253–1260.
[44] T. Bechert, P. Steinrücke, J.P. Guggenbichler, A new method for screening anti-infective biomaterials, Nat. Med. 6 (9) (2000) 1053–1056.
[45] C.S. Lee, H.S. Hwang, S. Kim, J. Fan, T. Aghaloo, M. Lee, Inspired by nature: facile design of nanoclay-organic hydrogel bone sealant with multifunctional properties for robust bone regeneration, Adv. Funct. Mater. 30 (43) (2020).
[46] W. Zhang, C. Ling, A. Zhang, H. Liu, Y. Jiang, X. Li, R. Sheng, Q. Yao, J. Chen, An all-silk-derived functional nanosphere matrix for sequential biomolecule delivery and in situ osteochondral regeneration, Bioact. Mater. 5 (4) (2020) 832–843.
[47] F.S. Pashaki, M. Nikpassand, Synthesis of novel azo-linked 5-amino-pyrazole-4-carbonitrile derivatives using tannic acid-functionalized silica-coated Fe3O4 nanoparticles as a novel, green, and magnetically separable catalyst, Front. Chem. 9 (2021).
[48] Z. Xia, A. Singh, W. Kiratitanavit, R. Mosurkal, J. Kumar, R. Nagarajan, Unraveling the mechanism of thermal and thermo-oxidative degradation of tannic acid, Thermochim. Acta 605 (2015) 77–85.
[49] X. Liang, K. Cao, W. Li, X. Li, D.J. McClements, K. Hu, Tannic acid-fortified zein-pectin nanoparticles: stability, properties, antioxidant activity, and in vitro digestion, Food Res. Int. 145 (2021), 110425.
[50] S.S. Chauhan, A.B. Shetty, E. Hatami, P. Chowdhury, M.M. Yallapu, Pectin-Tannic acid nano-complexes promote the delivery and bioactivity of drugs in pancreatic cancer cells, Pharmaceutics 12 (3) (2020).

[51] K.L. Worthington, A. Adamcakova-Dodd, A. Wongrakpanich, I.A. Mudunkotuwa, K.A. Mapuskar, V.B. Joshi, C. Allan Guymon, D.R. Spitz, V.H. Grassian, P. S. Thorne, A.K. Salem, Chitosan coating of copper nanoparticles reduces in vitro toxicity and increases inflammation in the lung, Nanotechnology 24 (39) (2013), 395101.
[52] H. Veisi, M. Pirhayati, A. Kakanejadifard, P. Mohammadi, M.R. Abdi, J. Gholami, S. Hemmati, In situ green synthesis of Pd nanoparticles on tannic acid-modified magnetite nanoparticles as a green reductant and stabilizer agent: its application as a recyclable nanocatalyst (Fe3O4@TA/Pd) for reduction of 4-nitrophenol and suzuki reactions, ChemistrySelect 3 (6) (2018) 1820–1826.
[53] H. Sehaqui, Y. Brahmi, W. Ju, Facile and universal method for the synthesis of metal nanoparticles supported onto carbon foams, Cellulose 27 (1) (2019) 263–271.
[54] M. McGill, J.M. Coburn, B.P. Partlow, X. Mu, D.L. Kaplan, Molecular and macro-scale analysis of enzyme-crosslinked silk hydrogels for rational biomaterial design, Acta Biomater. 63 (2017) 76–84.
[55] O. Hasturk, K.E. Jordan, J. Choi, D.L. Kaplan, Enzymatically crosslinked silk and silk-gelatin hydrogels with tunable gelation kinetics, mechanical properties and bioactivity for cell culture and encapsulation, Biomaterials 232 (2020), 119720.
[56] H. Chen, Q. Han, C. Wang, Y. Liu, B. Chen, J. Wang, Porous scaffold design for additive manufacturing in orthopedics: a review, Front. Bioeng. Biotechnol. 8 (2020) 609.
[57] V.G. Muir, T.H. Qazi, J. Shan, J. Groll, J.A. Burdick, Influence of microgel fabrication technique on granular hydrogel properties, ACS Biomater. Sci. Eng. 7 (9) (2021) 4269–4281.
[58] M.E. Villanueva, A.M. Diez, J.A. González, C.J. Pérez, M. Orrego, L. Piehl, S. Teves, G.J. Copello, Antimicrobial activity of starch hydrogel incorporated with copper nanoparticles, ACS Appl. Mater. Interfaces 8 (25) (2016) 16280–16288.
[59] J. Liao, T. Tian, S. Shi, X. Xie, Q. Ma, G. Li, Y. Lin, The fabrication of biomimetic biphasic CAN-PAC hydrogel with a seamless interfacial layer applied in osteochondral defect repair, Bone. Res. 5 (2017).
[60] J. Diao, H. Ding, M. Huang, X. Fu, F. Zou, T. Li, N. Zhao, C. Mao, Y. Wang, Bone defect model dependent optimal pore sizes of 3D-plotted beta-tricalcium phosphate scaffolds for bone regeneration, Small Methods 3 (11) (2019).
[61] Q. Zhang, H. Lu, N. Kawazoe, G. Chen, Pore size effect of collagen scaffolds on cartilage regeneration, Acta Biomater. 10 (5) (2014) 2005–2013.
[62] R. Li, H. Fan, L. Shen, L. Rao, J. Tang, S. Hu, H. Lin, Inkjet printing assisted fabrication of polyphenol-based coating membranes for oil/water separation, Chemosphere 250 (2020), 126236.
[63] Y. Ke, Y.J. Wang, L. Ren, Q.C. Zhao, W. Huang, Modified PHBV scaffolds by in situ UV polymerization: structural characteristic, mechanical properties and bone mesenchymal stem cell compatibility, Acta Biomater. 6 (4) (2010) 1329–1336.
[64] W. Zhang, C. Ling, X. Li, R. Sheng, H. Liu, A. Zhang, Y. Jiang, J. Chen, Q. Yao, Cell-free biomimetic scaffold with cartilage extracellular matrix-like architectures for in situ inductive regeneration of osteochondral defects, ACS Biomater. Sci. Eng. 6 (12) (2020) 6917–6925.
[65] J. Patterson, R. Siew, S.W. Herring, A.S. Lin, R. Guldberg, P.S. Stayton, Hyaluronic acid hydrogels with controlled degradation properties for oriented bone regeneration, Biomaterials 31 (26) (2010) 6772–6781.
[66] H. Zhang, L. Zhou, W. Zhang, Control of scaffold degradation in tissue engineering: a review, Tissue Eng. B Rev. 20 (5) (2014) 492–502.
[67] W. Zhang, Y. Zhang, A. Zhang, C. Ling, R. Sheng, X. Li, Q. Yao, J. Chen, Enzymatically crosslinked silk-nanosilicate reinforced hydrogel with dual-lineage bioactivity for osteochondral tissue engineering, Mater Sci Eng C Mater Biol Appl 127 (2021), 112215.
[68] M. Bartmański, Ł. Pawłowski, G. Strugała, A. Mielewczyk-Gryń, A. Zieliński, Properties of nanohydroxyapatite coatings doped with nanocopper, obtained by electrophoretic deposition on Ti13Zr13Nb alloy, Materials 12 (22) (2019).
[69] S. Xu, Q. Wu, Y. Guo, C. Ning, K. Dai, Copper containing silicocarnotite bioceramic with improved mechanical strength and antibacterial activity, Mater Sci Eng C Mater Biol Appl 118 (2021), 111493.
[70] M.A. Gwak, B.M. Hong, J.M. Seok, S.A. Park, W.H. Park, Effect of tannic acid on the mechanical and adhesive properties of catechol-modified hyaluronic acid hydrogels, Int. J. Biol. Macromol. 191 (2021) 699–705.
[71] C. Zhang, B.H. Wu, Y.S. Zhou, F. Zhou, W.M. Liu, Z.K. Wang, Mussel-inspired hydrogels: from design principles to promising applications, Chem. Soc. Rev. 49 (11) (2020) 3605–3637.
[72] P. Makvandi, G.W. Ali, F. Della Sala, W.I. Abdel-Fattah, A. Borzacchiello, Hyaluronic acid/corn silk extract based injectable nanocomposite: a biomimetic antibacterial scaffold for bone tissue regeneration, Mater Sci Eng C Mater Biol Appl 107 (2020), 110195.
[73] V. Perez-Silos, N.K. Moncada-Saucedo, V. Pena-Martinez, J. Lara-Arias, I. A. Marino-Martinez, A. Camacho, V.J. Romero-Diaz, M. Lara Banda, A. Garcia-Ruiz, A. Soto-Dominguez, H. Rodriguez-Rocha, N. Lopez-Serna, R.S. Tuan, H. Lin, L. Fuentes-Mera, A cellularized biphasic implant based on a bioactive silk fibroin promotes integration and tissue organization during osteochondral defect repair in a porcine model, Int. J. Mol. Sci. 20 (20) (2019).
[74] J. Luo, J. Yang, X. Zheng, X. Ke, Y. Chen, H. Tan, J. Li, A highly stretchable, real-time self-healable hydrogel adhesive matrix for tissue patches and flexible electronics, Adv Healthc Mater 9 (4) (2020), e1901423.
[75] S. Alizadeh, B. Seyedalipour, S. Shafieyan, A. Kheime, P. Mohammadi, N. Aghdami, Copper nanoparticles promote rapid wound healing in acute full thickness defect via acceleration of skin cell migration, proliferation, and neovascularization, Biochem. Biophys. Res. Commun. 517 (4) (2019) 684–690.
[76] J. Wang, X. Zhu, X. Li, W. Wang, X. Wang, L. Liu, Q. Deng, G. Bai, J. Wang, H. Feng, Z. Wang, G. Liu, Effects of copper on proliferation and autocrine secretion of insulin-like growth factor-1 (IGF-1) and IGF-binding protein-3 (IGFBP-3) in chondrocytes from newborn pigs in vitro, Biol. Trace Elem. Res. 144 (1–3) (2011) 588–596.
[77] D. Seliktar, Designing cell-compatible hydrogels for biomedical applications, Science 336 (6085) (2012) 1124–1128.
[78] C. Kaweeteerawat, C.H. Chang, K.R. Roy, R. Liu, R. Li, D. Toso, H. Fischer, A. Ivask, Z. Ji, J.I. Zink, Z.H. Zhou, G.F. Chanfreau, D. Telesca, Y. Cohen, P. A. Holden, A.E. Nel, H.A. Godwin, Cu nanoparticles have different impacts in Escherichia coli and lactobacillus brevis than their microsized and ionic analogues, ACS Nano 9 (7) (2015) 7215–7225.
[79] Z. Jiao, Q. Huo, X. Lin, X. Chu, Z. Deng, H. Guo, Y. Peng, S. Lu, X. Zhou, X. Wang, B. Wang, Drug-free contact lens based on quaternized chitosan and tannic acid for bacterial keratitis therapy and corneal repair, Carbohydr. Polym. 286 (2022), 119314-119314.
[80] S.N. Rath, A. Brandl, D. Hiller, A. Hoppe, U. Gbureck, R.E. Horch, A. R. Boccaccini, U. Kneser, Bioactive copper-doped glass scaffolds can stimulate endothelial cells in co-culture in combination with mesenchymal stem cells, PLoS One 9 (12) (2014), e113319.
[81] C.T. Wu, Y.H. Zhou, M.C. Xu, P.P. Han, L. Chen, J. Chang, Y. Xiao, Copper-containing mesoporous bioactive glass scaffolds with multifunctional properties of angiogenesis capacity, osteostimulation and antibacterial activity, Biomaterials 34 (2) (2013) 422–433.
[82] Y.H. Zhou, S.W. Han, L. Xiao, P.P. Han, S.F. Wang, J. He, J. Chang, C.T. Wu, Y. Xiao, Accelerated host angiogenesis and immune responses by ion release from mesoporous bioactive glass, J. Mater. Chem. B 6 (20) (2018) 3274–3284.
[83] S. Yang, J. Ji, M. Luo, H. Li, Z. Gao, Poly(tannic acid) nanocoating based surface modification for construction of multifunctional composite CeO(2)NZs to enhance cell proliferation and antioxidative viability of preosteoblasts, Nanoscale 13 (38) (2021) 16349–16361.
[84] C. Steffi, Z. Shi, C.H. Kong, S.W. Chong, D. Wang, W. Wang, Use of polyphenol tannic acid to functionalize titanium with strontium for enhancement of osteoblast differentiation and reduction of osteoclast activity, Polymers 11 (8) (2019).
[85] E.A. Makris, R.F. MacBarb, D.J. Responte, J.C. Hu, K.A. Athanasiou, A copper sulfate and hydroxylysine treatment regimen for enhancing collagen cross-linking and biomechanical properties in engineered neocartilage, Faseb. J. 27 (6) (2013) 2421–2430.
[86] C. Xu, J. Chen, L. Li, X. Pu, X. Chu, X. Wang, M. Li, Y. Lu, X. Zheng, Promotion of chondrogenic differentiation of mesenchymal stem cells by copper: implications for new cartilage repair biomaterials, Mater Sci Eng C Mater Biol Appl 93 (2018) 106–114.
[87] G. Li, T. Cheng, X. Yu, The impact of trace elements on osteoarthritis, Front. Med. 8 (2021), 771297.
[88] S.M. Bartell, H.N. Kim, E. Ambrogini, L. Han, S. Iyer, S. Serra Ucer, P. Rabinovitch, R.L. Jilka, R.S. Weinstein, H. Zhao, C.A. O'Brien, S.C. Manolagas, M. Almeida, FoxO proteins restrain osteoclastogenesis and bone resorption by attenuating H2O2 accumulation, Nat. Commun. 5 (2014), 3773.
[89] F. Loi, L.A. Cordova, J. Pajarinen, T.H. Lin, Z. Yao, S.B. Goodman, Inflammation, fracture and bone repair, Bone 86 (2016) 119–130.
[90] M. Li, H. Yin, Z. Yan, H. Li, J. Wu, Y. Wang, F. Wei, G. Tian, C. Ning, H. Li, C. Gao, L. Fu, S. Jiang, M. Chen, X. Sui, S. Liu, Z. Chen, Q. Guo, The immune microenvironment in cartilage injury and repair, Acta Biomater. 140 (2022) 23–42.
[91] L. Gong, J. Li, J.W. Zhang, Z.Y. Pan, Y.S. Liu, F.F. Zhou, Y. Hong, Y.J. Hu, Y.Q. Gu, H.W. Ouyang, X.H. Zou, S.F. Zhang, An interleukin-4-loaded bi-layer 3D printed scaffold promotes osteochondral regeneration, Acta Biomater. 117 (2020) 246–260.
[92] Y. Hu, Z. Gui, Y. Zhou, L. Xia, K. Lin, Y. Xu, Quercetin alleviates rat osteoarthritis by inhibiting inflammation and apoptosis of chondrocytes, modulating synovial macrophages polarization to M2 macrophages, Free Radic. Biol. Med. 145 (2019) 146–160.
[93] J. Riegger, R.E. Brenner, Evidence of necroptosis in osteoarthritic disease: investigation of blunt mechanical impact as possible trigger in regulated necrosis, Cell Death Dis. 10 (10) (2019) 683.
[94] J. Yeo, J. Lee, S. Yoon, W.J. Kim, Tannic acid-based nanogel as an efficient anti-inflammatory agent, Biomater Sci 8 (4) (2020) 1148–1159.
[95] M.K. Reumann, O. Strachna, S. Yagerman, D. Torrecilla, J. Kim, S.B. Doty, L. Lukashova, A.L. Boskey, P. Mayer-Kuckuk, Loss of transcription factor early growth response gene 1 results in impaired endochondral bone repair, Bone 49 (4) (2011) 743–752.
[96] T. Press, S. Viale-Bouroncle, O. Felthaus, M. Gosau, C. Morsczeck, EGR1 supports the osteogenic differentiation of dental stem cells, Int. Endod. J. 48 (2) (2015) 185–192.
[97] M. Elsafadi, M. Manikandan, R.A. Dawud, N.M. Alajez, R. Hamam, M. Alfayez, M. Kassem, A. Aldahmash, A. Mahmood, Transgelin is a TGFbeta-inducible gene that regulates osteoblastic and adipogenic differentiation of human skeletal stem cells through actin cytoskeleston organization, Cell Death Dis. 7 (8) (2016), e2321.
[98] E. Knierim, H. Hirata, N.I. Wolf, S. Morales-Gonzalez, G. Schottmann, Y. Tanaka, S. Rudnik-Schoeneborn, M. Orgeur, K. Zerres, S. Vogt, A. van Riesen, E. Gill, F. Seifert, A. Zwirner, J. Kirschner, H.H. Goebel, C. Huebner, S. Stricker, D. Meierhofer, W. Stenzel, M. Schuelke, Mutations in subunits of the activating signal cointegrator 1 complex are associated with prenatal spinal muscular

atrophy and congenital bone fractures, Am. J. Hum. Genet. 98 (3) (2016) 473–489.
[99] H. He, X.-l. Liu, H.-l. Zhang, J. Yang, F.-b. Niu, Z.-x. Li, Y. Liu, L. Chen, SNV and haplotype analysis reveals new CSRP1 variants associated with growth and carcass traits, Gene 522 (2) (2013) 206–213.
[100] B. Lilly, K.A. Clark, M. Yoshigi, S. Pronovost, M.-L. Wu, M. Periasamy, M. Chi, R. J. Paul, S.-F. Yet, M.C. Beckerle, Loss of the serum response factor cofactor, cysteine-rich protein 1, attenuates neointima formation in the mouse, Arterioscler. Thromb. Vasc. Biol. 30 (4) (2010), 694-U112.
[101] S. Weeks, A. Kulkarni, H. Smith, C. Whittall, Y. Yang, J. Middleton, The effects of chemokine, adhesion and extracellular matrix molecules on binding of mesenchymal stromal cells to poly(L-lactic acid), Cytotherapy 14 (9) (2012) 1080–1088.
[102] M. Bourens, F. Fontanesi, I.C. Soto, J.J. Liu, A. Barrientos, Redox and reactive oxygen species regulation of mitochondrial cytochrome c oxidase biogenesis, Antioxidants Redox Signal. 19 (16) (2013) 1940–1952.
[103] Q. Lu, B. Zhang, M. Li, B. Zuo, D.L. Kaplan, Y. Huang, H. Zhu, Degradation mechanism and control of silk fibroin, Biomacromolecules 12 (4) (2011) 1080–1086.